Journal of Applied Geophysics 205 (2022) 104778

Contents lists available at ScienceDirect

Journal of Applied Geophysics

journal homepage: www.elsevier.com/locate/jappgeo

An expeditious approach for slope stability assessment using integrated 2D electrical resistivity tomography and unmanned aerial vehicle survey

Muhammad Junaid [a,b], Rini Asnida Abdullah [a,*], Radzuan Saa'ri [a], Mohd Nur Asmawisham Alel [a]

[a] School of Civil Engineering, Universiti Teknologi Malaysia, 81310 Skudai, Johor Bahru, Malaysia
[b] Department of Mining Engineering, Karakoram International University, Main Campus, University Road, Gilgit 15100, Pakistan

ARTICLE INFO

Keywords:
Slope stability assessment
2D ERT survey
UAV survey
Slope failure
Kinematic analysis

ABSTRACT

A comprehensive slope stability assessment of two sites, namely Site 1 and Site 2, has been conducted. An integrated Unmanned Aerial Vehicle Survey (UAV) and 2D Electrical Resistivity Tomography (2D ERT) survey at both sites were carried out. The rock mass quality using Rock Quality Designation (RQD) system was quantified, and discontinuity orientations were obtained from the UAV point cloud. The obtained discontinuity orientations were utilized to identify possible geometric failures such as planar, flexure and wedge. The 2D ERT survey at both sites was deployed to discern subsurface lithology. Based on the UAV survey, Site 1 slope was prone to flexure toppling and wedge failure. While few intersections at Site 2 were favourable for Wedge formations. 2D ERT survey reported four geological layers as water-saturated zone or clay layer (200–300 Ωm), highly fractured rock (400–700 Ωm), fractured rock (800–2200 Ωm) and fresh rock (>2200 Ωm) at both study sites. Combining the information of both techniques, the rock mass at Site 1 is moderately fractured to fresh rock. However, the top portion of Site 1 is highly fractured as compared to the lower portion. The rock quality at Site 2 is moderate to highly fractured rock mass. The integrated approach applied in this research study was proven expeditious, inexpensive and rapid for comprehensive slope stability assessment.

1. Introduction

Slope stability assessment in recent few decades is getting greater interest in response to the construction of extensive road networks and residential areas in the hilly and mountainous region due to population expansion and socio-economic development. Malaysia also has 25% of the terrain hilly and mountainous (Haliza Abdul Rahmana, 2017). Consequently, a substantial portion of highways and residential areas in Malaysia are exposed to the threat of slope failure. Slope failure contributes to 8.3% of all-natural disasters in Malaysia, causing 500 fatalities to date (Rahman and Mapjabil, 2017). Therefore, a comprehensive slope stability assessment is crucial to mitigate slope failure, particularly along the roadside, thus reducing the loss of life, damage to property and socio-economic impact.

Slope stability assessments in this research study were carried out at two study sites, namely Site 1 and Site 2. Site 1 lies in Ipoh, Perak, along the North-south expressway in the western peninsular, serving as a backbone of the west coast. Site 2 exists alongside the highway adjacent to the industrial zone (*Pengerang* Integrated Petroleum Complex), Pengerang, Johor, Malaysia. Considering the socio-economic importance of both highways, a sound mitigation strategy for any foreseeable slope failure is required to avoid the disruption of transportation and loss of lives.

A comprehensive and precise slope stability assessments need to understand several parameters. These parameters include the understanding of analysis of geologic discontinuities and physical characteristics of the rock slope. Measurements of geological discontinuities involve orientations, persistence, spacing and roughness of joints and faults. In contrast, the physical characteristics encompass the slope height, slope length, face angle, identification of various lithological features and measuring the magnitude of driving and resistive forces (Azarafza et al., 2020; Erguler et al., 2020; Khanna and Dubey, 2021; Sadeghi et al., 2020). Therefore, rock slope stability assessment techniques are broadly categorized as kinematic analysis, numerical modelling, limit equilibrium analysis and empirical methods (Gurocak et al., 2008).

This article mainly focuses on kinematic and empirical methods. In a jointed rock mass, the stability of the rock slope is mainly controlled by joint orientations (Smith and Holden, 2021). The orientation of the joints with respect to the slope face determines the kinematic stability of

* Corresponding author.
E-mail address: Asnida@utm.my (R.A. Abdullah).

https://doi.org/10.1016/j.jappgeo.2022.104778
Received 17 August 2021; Received in revised form 3 July 2022; Accepted 8 August 2022
Available online 11 August 2022

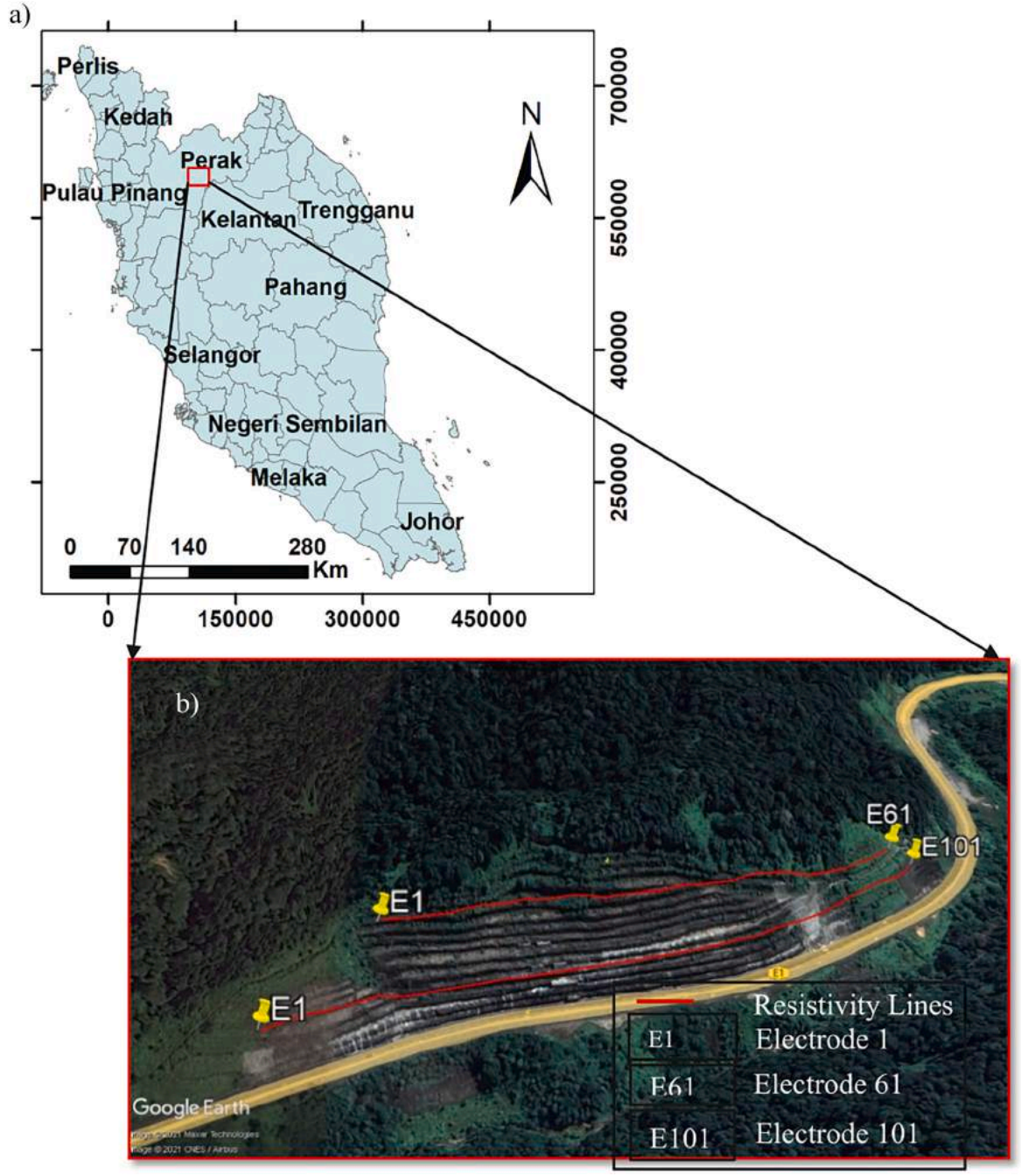

Fig. 1. a) Map of peninsular Malaysia b) Site 1.

a slope. Kinematic techniques assess the slope stability by identifying the geometric formation of various types of failures (Planar, wedge, direct and flexure toppling) that occur due to the presence of unfavorably oriented discontinuities (Gurocak et al., 2008). While the empirical method or rock mass classification system quantitively describe the engineering behaviour of rock mass condition (Morales et al., 2019). Rock quality designation (RQD) classification system developed quickly for slope stability assessment because it can be simply, inexpensively, and rapidly obtained as compared to other rock mass classification systems (Chen and Yin, 2019; Haftani et al., 2016; Zhang and Einstein, 2004; Zheng et al., 2018). The degree of fracturing of rock mass using RQD can be measured via direct techniques (drill cores) and indirect techniques such as fracture frequency (λ) and volumetric joint count (Jv) (W. Zhang et al., 2012; Zheng et al., 2018). In this article, the RQD was calculated using an indirect technique due to its low cost, simplicity and reproducibility as compared to coring (Haftani et al., 2016).

In recent decades, technological advancement has enabled to obtain joint orientations and Jv more quickly and efficiently, using various remote sensing techniques such as Unmanned Aerial Vehicle (UAV), Interferometric Synthetic Aperture Radar (InSAR), Light Detection and Ranging (LiDAR), and Terrestrial Laser Scanning (TLS) (Albarelli et al., 2021). Currently, UAVs have proven it significance for slope stability assessment because it is the best compromise between price and efficiency among all remote sensing techniques (Guisado-Pintado et al., 2019). The increasing application of UAV for slope stability assessment is due to its precise data collection ability, easy interpretation, and the possibility of various views such as vertical, 3D and oblique. The ability of UAV surveys to obtain high-resolution 3D models, which allows the

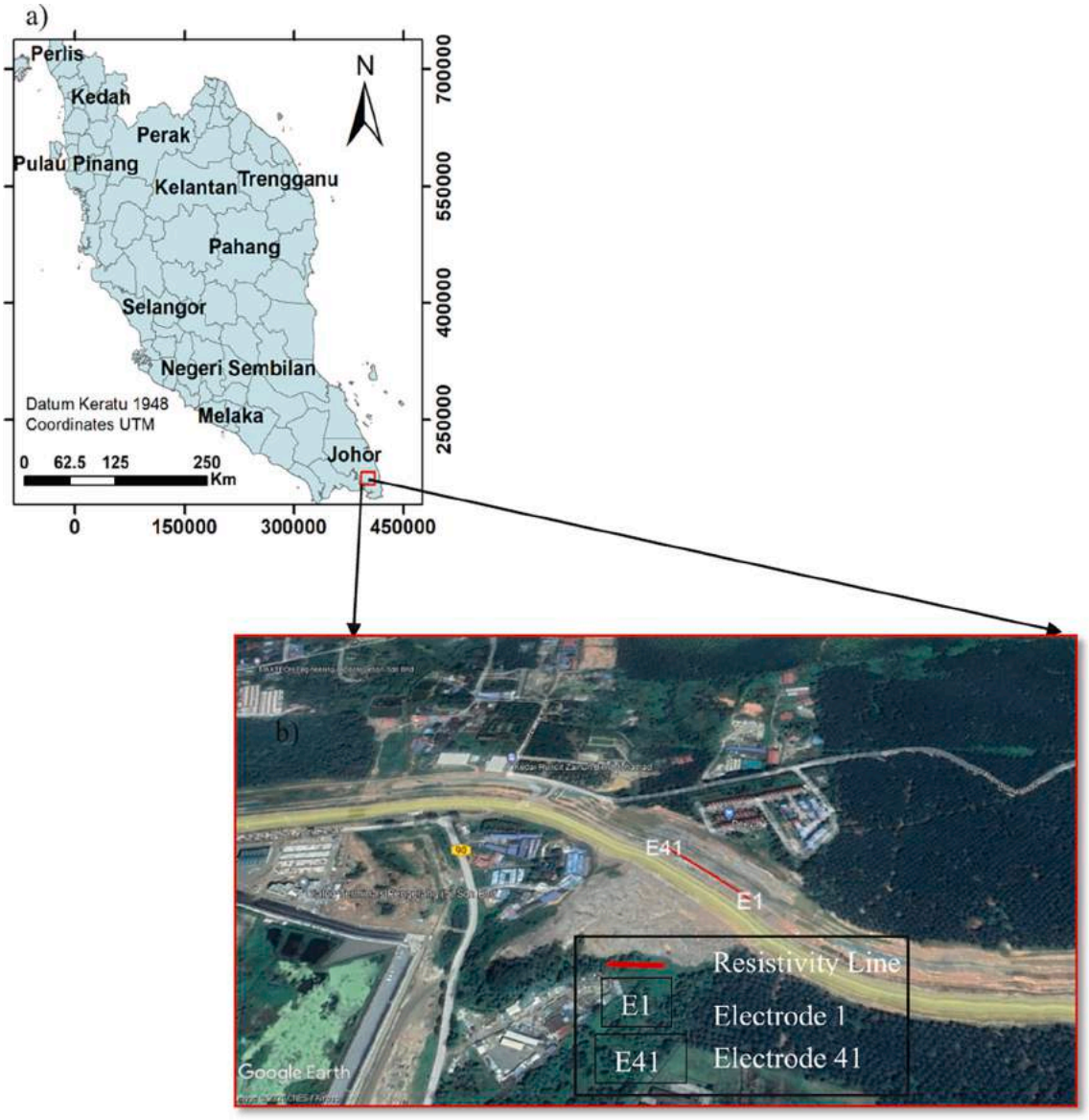

Fig. 2. a) Map of Peninsular Malaysia b) Site 2.

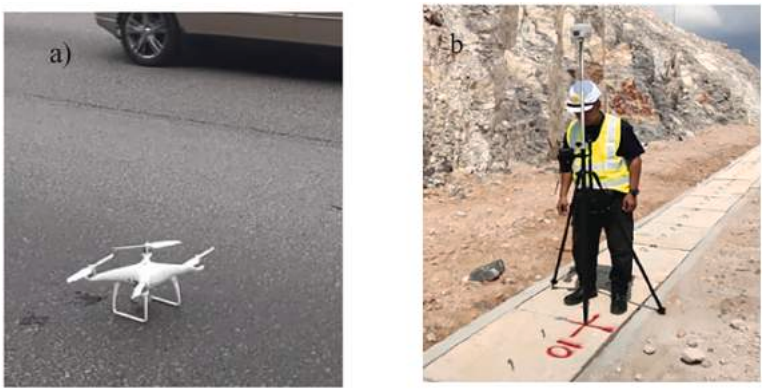

Fig. 3. UAV and GCP survey a) DJI Phantom 4 v2.0 UAV system b) SOUTH G1 GNNS system.

extraction of accurate geometric information, also favours its application for slope stability assessment (Albarelli et al., 2021). The UAV captured a series of aerial images of the area of investigation, and each photograph is stored with geotags (coordinates and orientation information). This allows for georeferentiation of a point cloud obtained from digital photogrammetry reconstruction algorithms (Bar et al., 2020;

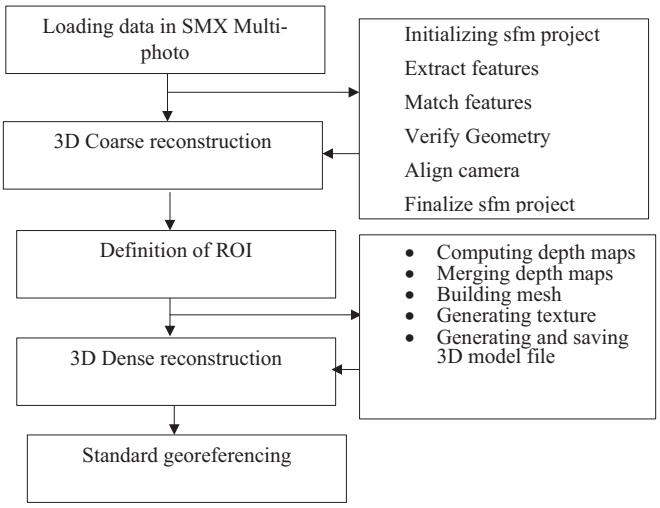

Fig. 4. Steps used by SMX to reconstruct 3D point cloud.

Colomina and Molina, 2014; Lee and Choi, 2016; Park and Choi, 2020). The obtained DTM (digital terrain model) and DSM (digital surface model) enable us to assess the stability of the slope. UAV was efficiently utilized to identify various structure planes and unstable block using the RANSAC algorithm (Wang et al., 2019a). The kinematic, limit equilibrium method (LEM) and numerical analysis of the rock slope using a UAV survey can be found in various literature (Bar et al., 2020; Barlow et al., 2017; Török et al., 2018; Wang et al., 2019b). Although theses research work successfully identifies the types of failure, the slope surface condition and loose block along the rock slope, the subsurface lithology was not considered in all the previous research work because the UAV point cloud provides surface assessment only. In many cases, the existence of highly conductive subsurface geological layers such as clay or water-saturated zone is also the main source of slope failure. This means for a detailed assessment of slope instabilities, a detailed characterization of both the ground surface and subsurface kinematic is prerequisite (Buša et al., 2020). In addition, the calculation of RQD on a 3D point cloud is not possible if the rock slope surface is covered with vegetation or any loose material.

Table 1
GCP accuracy assessment of Site 1.

GCP point	Rx (m)	Ry (m)	Rz (m)
GCP1	0.019	−0.006	−0.007
GCP2	−0.015	−0.015	0.014
GCP4	−0.029	−0.038	−0.056
GCP5	0.031	0.005	0.047
GCP14	0.008	0.032	0.004
GCP15	−0.005	−0.005	−0.003

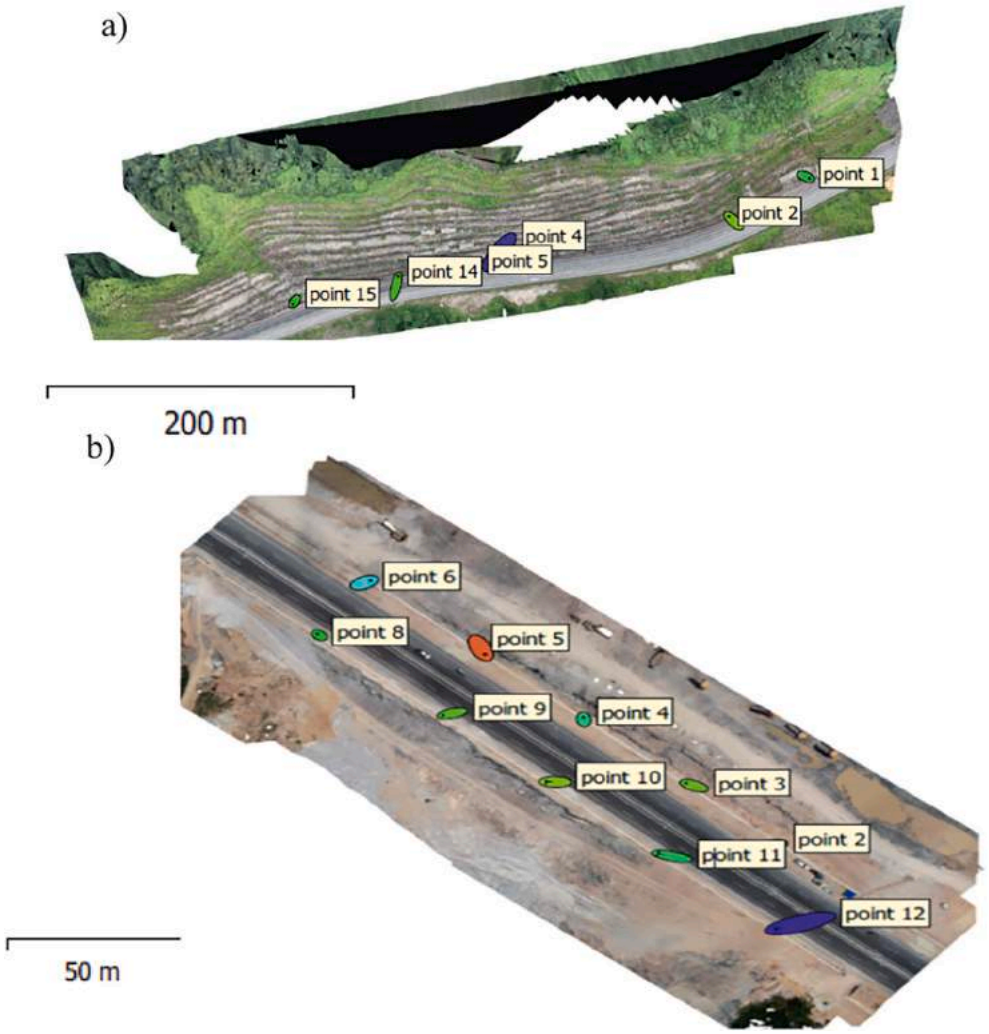

Fig. 5. GCPs points and 3D point clouds a) Site 1, b) Site 2.

Table 2
GCP accuracy assessment of Site 2.

GCP point	Rx (m)	Ry (m)	Rz (m)
GCP2	0.007	0.003	−0.005
GCP3	−0.008	0.003	0.004
GCP4	−0.004	0.003	−0.007
GCP5	0.004	−0.008	0.021
GCP6	0.006	0.003	−0.012
GCP8	−0.061	0.059	0.012
GCP9	−0.009	−0.002	0.003
GCP10	0.021	−0.016	0.008
GCP11	0.022	−0.046	−0.061
GCP12	0.018	0.003	0.041

Table 3
Detail of resistivity lines.

Site	Survey line	No of electrodes	Electrode spacing (m)	Direction	Location on rock slope
Site 1	L1	61	10	South west to north west	Top
	L2	101	10	South west to north west	Middle
Site 2	L3	41	3	North to South	Top

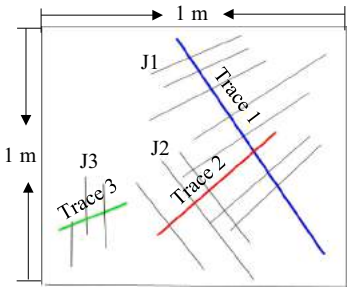

Fig. 6. 1*1 blocks representing joints and joint sets spacing.

To delineate the subsurface geology of the rock slope, 2D ERT provides a promising approach. Nevertheless, the 2D ERT survey may give ambiguous results by overlapping the resistivity values of various geological layers. However, the extensive application of 2D ERT for various geotechnical investigations globally proved it a reliable technique. An integrated geotechnical and geophysical technique is widely applied for the stability assessment of the slope (Khan et al., 2017; Rusydy et al., 2021). (Vanneschi et al., 2018) integrated 2D ERT and soil boring testing were employed to identify landslide failure mechanisms through LEM and finite element method (FEM). Numerous authors have applied 2D ERT in combination with boreholes to identify slope deformation and various lithological features (Falae et al., 2019; Mezerreg et al., 2019; Pasierb et al., 2019). The previous research provides a detailed subsurface geological assessment of the rock slope, but the approach is considered time-consuming and expensive due to coring. To add more, many steep slopes are risky for shifting heavy drilling equipment. Therefore, 2D ERT with UAV survey is now being employed globally to analyze the detailed surface and subsurface characterization of the rock slope (Buša et al., 2020; Samodra et al., n.d.). The fundamental principle of 2D ERT is the injection of galvanic current via a pair of contiguous current electrodes and measuring the potential difference across other twin electrodes subsequently (Egwuonwu et al., 2021; Kumari et al., 2021). The desired targeted depth is manipulated by increasing the electrode spacing; however, the resolution decreases (Loke, 1999; Loke et al., 2013). The widespread application of 2D ERT for geotechnical investigation is because it is simple, rapid, inexpensive and have ability of automated computerized data acquisition and processing (Ibraheem et al., 2021; Junaid et al., 2021; Sari et al., 2020).

This research work focuses on the integrated application of UAV and 2D ERT to provide a detailed slope stability assessment of the study area. The UAV survey was accomplished to analyze the rock mass condition of the slope surface and locate possible geometric failures along the rock slope. While the 2D ERT survey was deployed to characterize the subsurface lithology by locating the clay layer or water-saturated zone. The outcrop information obtained from the UAV survey and the subsurface geological interpretation of the 2D ERT survey were correlated to identify probable rock slope failure. The efficiency of both the techniques for slope stability assessment is also compared in this research study.

2. Geological study area

2.1. Site 1

The general geology of the study area is underlain by granitic bodies of Main Range Granite (JMG, 2014). The rock slope is a part of the Gunung Kledang range located in Kinta Valley. The study area is underlain by massive and homogeneous igneous granitic rock, which forms terrain with high reliefs and exceeding 700 m (CM, 2014). the Kledang Range is in the west of Kinta valley, about 40 km long. Fig. 1a shows the map of peninsular Malaysia, while Fig. 1b indicates the study area. The red lines in Fig. 1b illustrate the resistivity lines at the top and middle of the study area.

2.2. Site 2

Referring to "Johor Geological Map", by Mineral and Geoscience Department Malaysia, the general geology of the study area is underlain by granitic bodies with acidic intrusion having high content of silica (JMG, 2014). The granitic rock in the study area is composed of phyllite, shale, slate and subordinate sandstone and schist. Fig. 1a represents the map of peninsular Malaysia. The selected study site is along a highway shown in Fig. 2b. The elevation with respect to mean sea level at the selected site ranges 15–48 m having slope height from 10 to 15 m. The red line in Fig. 2b represents the resistivity line at the rock slope.

3. Methodology

This section provides details about the methodology applied to achieve the targeted objectives. Two types of surveys, UAV and 2D ERT were performed to assess the stability of rock slopes.

3.1. UAV survey data acquisition

The principal requirement of the UAV survey is to collect a set of aerial images with sufficient overlap to reconstruct an accurate 3D surface model from a point cloud with a resolution that captures the scale of significant features (Bar et al., 2020; Ekinci et al., 2021). This can be achieved by capturing aerial images with high-resolution cameras having no <60% overlap between adjacent images and at least three images per feature (Rodriguez et al., 2020). The UAV survey of both the study sites was carried out using DJI Phantom 4 v2.0 schematized in Fig. 3a. The system has a 0.02 m sensor camera capable of shooting a 20 MP photo. The maximum flight time is approximately 30 min having a maximum speed of 72 km/h. The vertical and horizontal hover accuracy of the system with GPS positioning is 0.5 m and 1.5 m, respectively (dji).

The images were captured at the height of approximately 180–260 m and 5–30 m at Site 1 and Site 2, respectively. At both sites, the ground control points (GCPs) were established using Real-Time Kinematic Global Navigation Satellite System (RTK GNSS) using the SOUTH G1 GNSS system shown in Fig. 3b. A total of 6 GCP points at Site 1 and 10

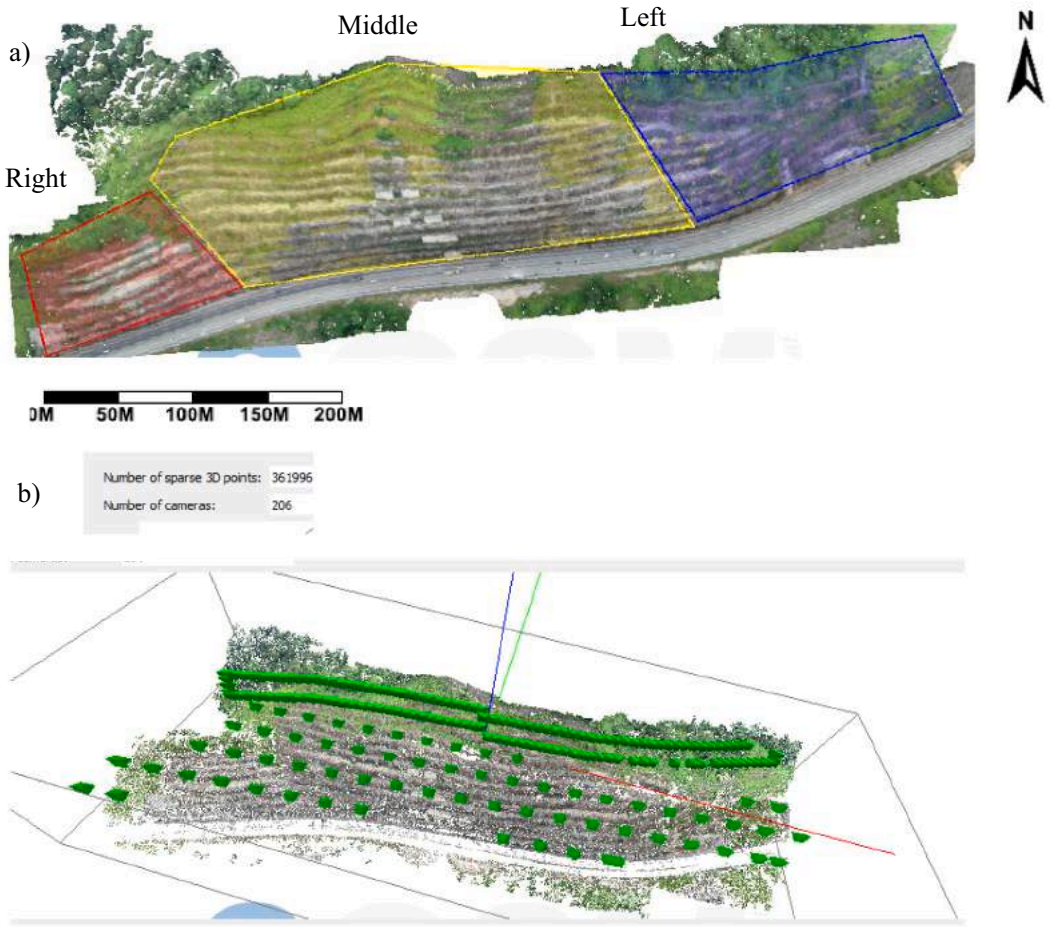

Fig. 7. 3D Point cloud of Site 1 a) 3D point cloud b) various camera positions used for capturing aerial images.

GCP points at Site 2 at slope toe were established for the georeferencing of the 3D models.

3.2. UAV data processing

The 3D point cloud was reconstructed from these captured images using ShapeMetriX (SMX) UAV software, following the steps as illustrated in Fig. 4 (3GSM, n.d.). The captured images were loaded into the SMX multiphoton to reconstruct the 3D coarse point cloud using the structure from motion (sfm) technique. The 3D Coarse reconstruction is a seven steps process. After reconstructing the 3D coarse point cloud, the region of interest (ROI) has opted manually, and a 3D dense point cloud is constructed. Finally, the georeferencing of the 3D point cloud was carried out using Universal Transverse Mercator (UTM).

The 3D point cloud of Site 1 was reconstructed from 245 images and was georeferenced using 6 GCPs see Fig. 5a. The accuracy of the GCPs is provided in Table 1. A total of 246 images were used to reconstruct the 3D point cloud of Site 2. 10 GCPs, as shown in Fig. 5b, were exploited for the georeferencing of the point cloud. The accuracy assessment of the GCPs is provided in Table 2.

3.3. 2D ERT Survey

2D ERT survey of both sites (Site 1 and Site 2) was accomplished using ABEM Ls Terameter. Before starting the 2D ERT survey, the number of electrodes and length of resistivity profile is required to be set according to the survey requirements. After this, the wire is spread, and all are incurred in the ground and connected to the wire. A trial experiment is carried out to confirm that all electrodes have sound contact with the ground and are connected to an electric cable. Then, after successful trial test, subsurface apparent resistivity data was acquired. The topographic profile of each resistivity line was constructed from the relative levels (or sea level readings) of each electrode point, respectively. Coordinates and elevation of each electrode were recorded.

The 2D ERT survey of Site 1 consisted of two lines, Line 1 and Line 2 shown in Fig. 1b by red lines. All the resistivity survey Lines (Line 2, Line 3) were laid longitudinal on top and middle of the rock slope at the mentioned area by single run and roll-along. The length of resistivity line L1 was 600 m and L2 1 km. the total number of 61 electrodes at L1 and 101 electrodes for L2 (one survey electrode) equally spaced at 10 m in Schlumberger protocol was utilized in this research work.

At Site 2 one resistivity line L3 was carried out. The length of the survey line was 120 m. A total number of 41 electrode (one center electrode) with 3 m spacing in Schlumberger protocol was utilized. The detail of the resistivity lines length, direction and electrode spacing of both sites are summarized in Table 3.

3.4. Calculation of RQD

The RQD at both sites were measured using indirect techniques to characterize the rock mass quality. The RQD using fracture frequency was measured by tracing a scanline and joints on the point cloud in SMX software. The joint set intersection of the scanline along the distance was recorded, and fracture frequency (λ) was calculated utilizing Eq.(1) (Awang et al., 2021; Rusydy et al., 2021).

To measure the degree of jointing of both sites, the RQD was also calculated using Jv. Three sections (3*3 m) at Site 1 and two at Site 2 were used. Each section was further divided in to a 1*1 m block. Next,

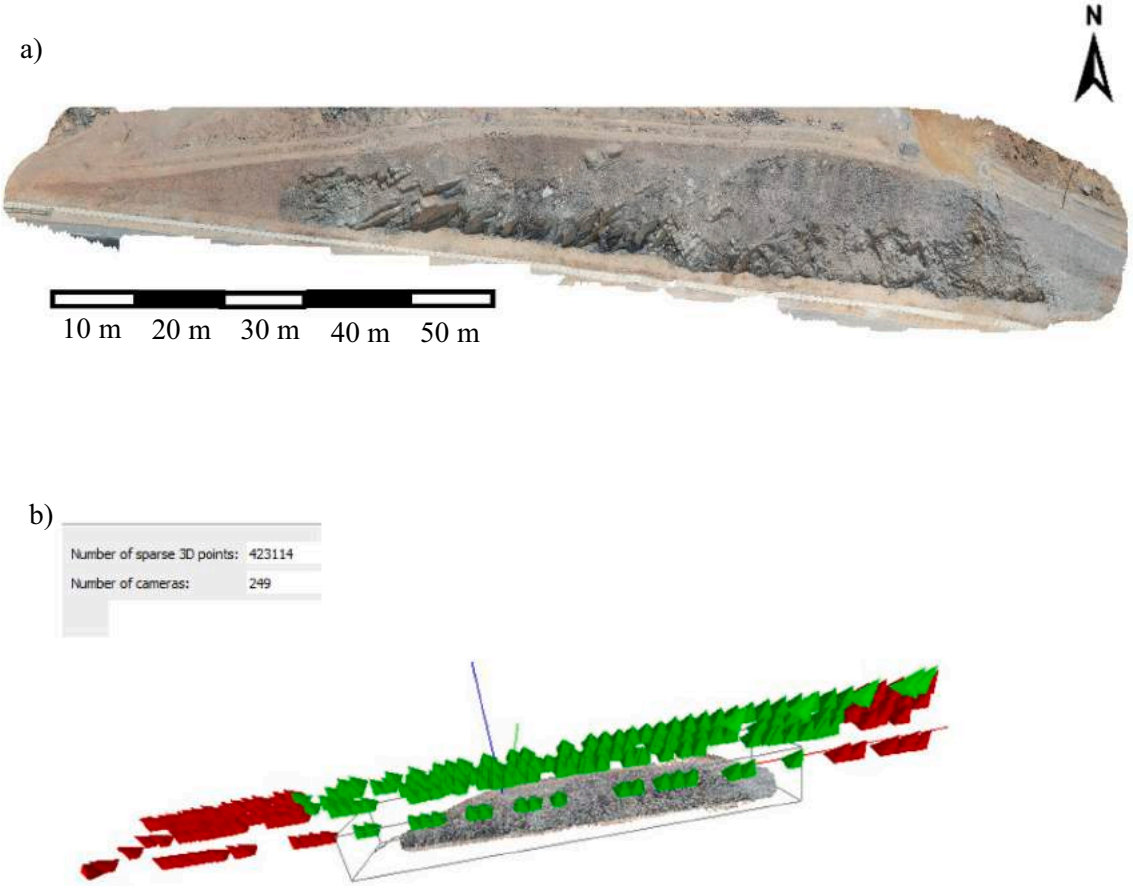

Fig. 8. 3D Point cloud of Site 2 a) 3D point cloud b) various camera positions used for capturing aerial Images.

the joints were traced in each block and a scanline was drawn (Fig. 6). The spacing between the joints was measured and RQD was calculated using Eq. (2) and Eq. (3) (Alameda-Hernández et al., 2019; Khanna and Dubey, 2021; Nanda et al., 2020; Singh et al., 2020).

$$RQD = 100e^{-0.1\lambda}(1+0.1\lambda) \quad (1)$$

$$RQD - 115 - 3.3Jv \quad (2)$$

$$RQD = 110 - 2.5Jv \quad (3)$$

3.5. Kinematic analysis

Various parameters such as joint orientations, slope height, and slope orientation required for kinematic analysis were obtained from the UAV point cloud using SMX UAV software. The discontinuity orientations (Dips and Dips Direction) were obtained by tracing joints in SMX software. The dips and dip directions of the slope face were obtained by fitting a plane to the average direction of the slope face. The obtained data i.e. geometrical attitude of slope and discontinuities orientation, was then further processed to identify the various types of potential failure (Planar, flexure toppling and wedge failure).

4. Results

In the section, the results obtained from the UAV and 2D ERT survey from both site (Site 1 and Site 2) are presented.

4.1. UAV survey

The obtained 3D Point cloud of Site 1 using SMX UAV software is shown in Fig. 7a. The 3D point cloud was constructed from 246 images, which were captured from 206 camera positions and 19346465 sparse 3D points Fig. 7b. In comparison, Fig. 8a represent the 3D Point cloud of Site 2. At Site 2, around 104 camera positions were used to capture the images shown in Fig. 8b. A total number of 245 images of enough resolution were captured to identify various geological features. The 3D points cloud of Site 2 was reconstructed using 9385817 sparse data points.

4.2. 2D ERT

2D ERT data processing was performed in zondres2D software (Zond, n.d.). The generation of 2D resistivity tomograph is a two-step process. Firstly, the geomodelling of the data using forward modelling followed by inversion (least square optimization technique) was carried out. In geomodelling, the subsurface is divided into a large number of rectangular cells, and the apparent resistivity value for each cell is calculated. The number and width of the cell was automatically done by the software. The data quality was improved by filtering the bad data points before inversion. The data iteration is carried out until the optimum RMS error is achieved. An RMS error of 5.15%, 10.1% and 3.49% were recorded after 13,13 and 10 iterations for resistivity lines L1, L2 and L3, respectively.

A total of 906 data points were recorded by resistivity line L1 from 787 cells. Resistivity values 200 Ωm to >13,000 Ωm were obtained at L1, depicted in Fig. 9a. The resistivity of the rock mass decreases with the degree of fracturing of the rock mass. Therefore, the geological layer having lower resistivity was categorized as fractured rock while the higher resistivity rock layer was identified as fresh rock (Ishak et al., 2020; Junaid et al., 2019; Lin et al., 2021; Olona et al., 2010). Based on the mentioned literature, a high portion of the subsurface beneath L1

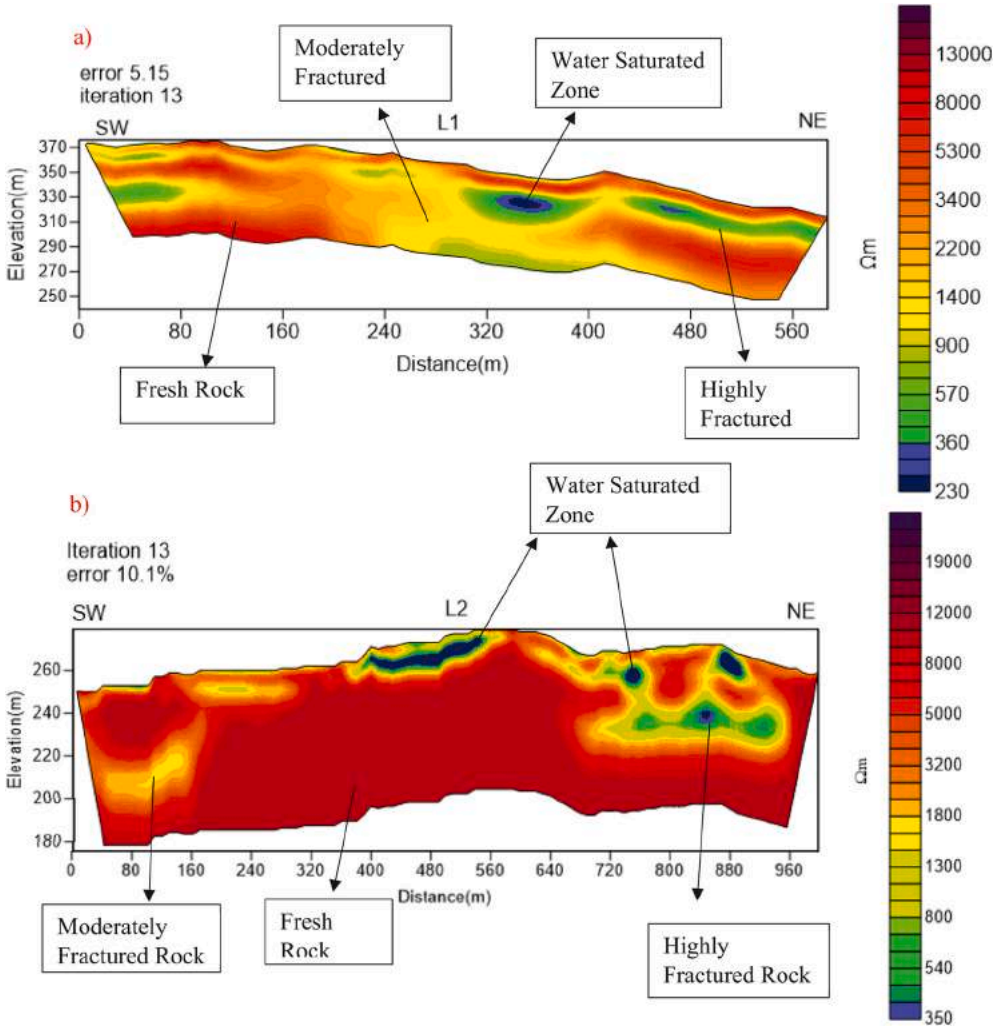

Fig. 9. 2D inverted resistivity images a) resistivity line on top of Site 1 b) resistivity line in the middle of Site 1.

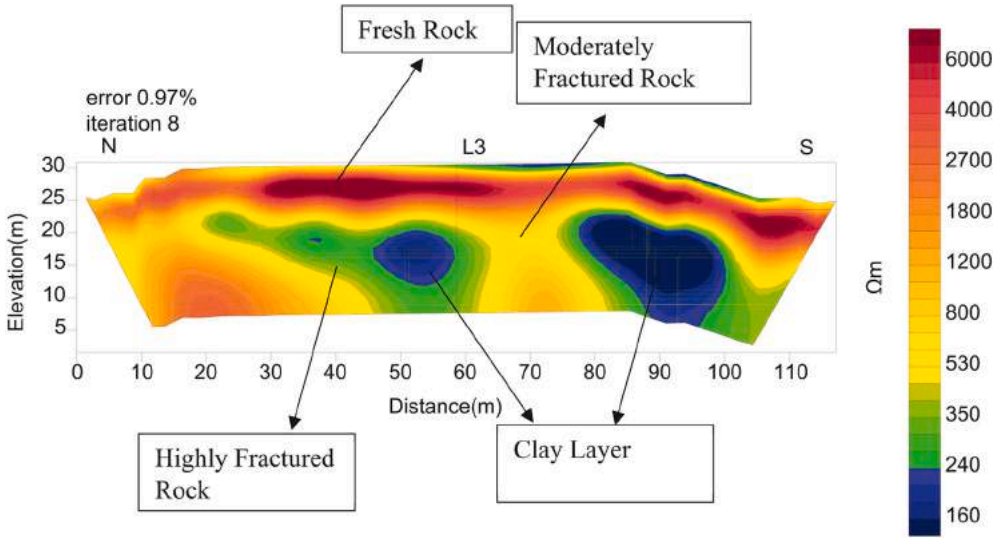

Fig. 10. Resistivity line on top of Site 2.

was found moderately fracture rock characterized by yellow color having resistivity ranges 1000–2200 Ωm. A low resistivity layer with resistivity 500–900 Ωm at both ends was also discerned. This layer is characterized as highly weathered rock represented by green color. Towards the Southwest direction, fresh rock at a depth of 15 m and 70 m were also identified. The fresh and strong rock is characterized as dark

Table 4
Determination of RQD using scanline survey for Site 1 and Site 2.

Site	Scanline	J1 ($\lambda 1$)	J2 ($\lambda 2$)	J3 ($\lambda 3$)	J4 ($\lambda 4$)	Fracture frequency (λ)	RQD	Remarks
Site 1	Scanline 1	6.5	2.2	4.15	2.1	14.95	55.95	Fair Rock
	Scanline 2	6.21	3.9	5.32		15.43	54.28	Fair Rock
	Scanline 3	2.42	2.92	2.9	1.41	9.64	77.03	Good Rock
Site 2	Scanline 1	5.34	4.58	6.92		16.84	49.82	Poor Rock
	Scanline 2	5.9	5.32	4.92		16.14	52.04	Fair Rock

Table 5
Discontinuity orientation at Site 1 and Site 2.

Study site	Joint set	Dips (^{0})	Dips direction (^{0})
Site 1	J1	74	180
	J2	83	276
	J3	84	22
	J4	73	86
Site 2	J1	87	194
	J2	70	38
	J3	27	79

red with resistivity values >2500 Ωm. A small portion of the low resistivity layer of 300 Ωm was also identified at the middle of Line L1.

The resistivity line L2 provided subsurface information using 1654 data points divided in to 4000 cells shown in Fig. 9b. The high portion of the rock mass at resistivity line L2 was a fresh rock with a resistivity value >2500 Ωm shown by dark red. Towards the north-east and South-west direction, a 15–20 m thick layer of moderately fracture rock were reported represented by yellow color having resistivity ranges 1000–2200 Ωm. At the middle of the line near the surface, a water-saturated zone of resistivity values 200–400 Ωm were also discerned. The water bearing strata was also noticed towards the left of the slope at the north-east direction.

The resistivity line L3 divided the subsurface in 1491 rectangular cells, enabling the obtain resistivity values for 524 data (Fig. 10). The resistivity Line L3 were carried at Bukit Ayam. The yellowish color represents fractured rock having resistivity ranges 1000–2200 Ωm. A fresh rock layer at a depth of 5 m having resistivity greater 2400 Ωm was characterized by dark red color was also reported by L3. A highly fractured rock at a depth of 10 m having resistivity ranges 400–1000 Ωm was identified throughout the study area. The resistivity layer with dark blue color shows the lowest resistivity values from 100 to 300 Ωm at 15 m depth. This layer is identified as a clay layer.

4.3. Obtained RQD values from various blocks

A total of 3 scanlines at each site were drawn, and RQD values of every scanline were calculated using eq. (1). The obtained values of the scanline survey at both sites are summarized in Table 4.

The RQD was also obtained using J_v exploiting eq. (2) and eq. (3) from 27 blocks at Site 1 and 18 Blocks at Site 2. The calculated Jv values at Site 1 vary between 9.47 and 19.31, corresponding to RQD values between 83 and 51. While at Site 2, the obtained Jv ranges between 17.99 and 21.87 refers to RQD value 42–55.

4.4. Kinematic analysis

The discontinuity orientations (Dips and Dips Direction) were extracted from 450 joints at Site 1 and 216 at Site 2. Four joint sets (J1, J2, J3, J4,) at Site 1 and three at Site 2 (J1, J2, J3) were identified. The obtained orientations of joint sets from both sites are tabulated in Table 5. The site 1 slope exhibits dip around 75^0 and a dip direction 25^0, while dips and dips direction of slope face at site 2 were 50^0 and 110^0 respectively. At Site 1 the rock slope was divided in to three sections right, middle and left, as represented in Fig. 7a by red, yellow and blue color, respectively.

The discontinuity orientation data were imported to the Dips 8 software to identify joint sets and perform kinematic analysis (Rocsciences, n.d.). The kinematic analysis for each section (right, middle and left) of site 1 is performed separately for various types of failure such as planar, wedge and flexure toppling. The kinematic analysis is performed using stereographic projection method (Park et al., 2016). This method includes plotting measured discontinuities as stereonet to evaluate the stability of the rock slope. Based on the kinematic analysis of the Site 1, the right and middle sections have no risk of planar failure, as depicted in Fig. 11(a) and 13. As shown in Fig. 11 (b), the right section of site 1 has no risk of wedge failure, but in the middle 9% of intersections, 11,834 out of 120,779 are favourable for wedge failure, as illustrated in Fig. 14. The wedge failure in the middle of site 2 results from the intersection of J2 and J4. Both the right and middle section of Site 1 is more prone to flexure toppling as manifested by stereonet representation in Fig. 12c and 15b. A total of 15 joints out of 75 joints, around 20% are critical for flexure toppling at the right section of site 1. At the same time, 68 joints out of 492 joints, around 13.82% cause flexure toppling in the middle section. Joint sets J1 is the most contributor to the flexure toppling.

At the left section of the slope, a small stream of runoff water was observed by visual inspection at Site 1. The 3D point cloud also identified this small stream of water (Fig. 22d). 2D ERT images also revealed small pockets of water-saturated zone at same location in Fig. 9b. The water saturation reduced the friction angle from around 4 to 5 degrees (Abdullah, n.d.; Barton and Choubey, 1977). Therefore, for the left section of the rock slope, kinematic analysis was performed for dry and saturated rock. Figs. 16 and 17 show that water saturation at Site 1 does not influence on planar and flexure toppling. The kinematic analysis of both dry and saturated rock for flexure and planar failure gives similar results. 1.04% and 20% of joints were reported critical for planar and flexure toppling in both cases. However, it is interesting to notice that the kinematic analysis of right and middle sections of the slope shows no risk of planar failure, while the left section of the slope exhibits a minimal (1.04%) risk for planar failure. It is, therefore, assumed that the planar failure in the left section results due to water saturation as in the kinematic analysis of the other sections the effect of moisturization was not considered. The wedge analysis of the left section is also worth noticing as the risk of wedge analysis increases from 4.86% (dry rock) to 6.86% (saturated rock) as shown in Fig. 18.

The kinematic analysis of Site 2 reveals that the rock slope is not susceptible to planar and flexure detachment, as shown in Fig. 19(a) and 19(b). However, 2688 out of 23,220, which is 11.5% of the intersection, are making a wedge see Fig. 20b. The intersection of J1 and J2 is causing wedge formation at site 2.

5. Discussion

As the estimation of RQD using Jv is more reliable compared to fracture frequency, therefore in this study, the data obtained from Jv is exploited for assessing the quality of rock mass at both sites. The obtained RQD using Eq. (2) and Eq. (3) are compared as depicted in Fig. 20 for both sites. The Jv values at Site 1 vary between 9.47 and 19.31. The graphical representation of RQD Vs Jv (Fig. 21a) for Site 1 showed a significant difference when the Jv values were higher, but a small difference was observed for the Jv values <10. On the other hand, the Jv of

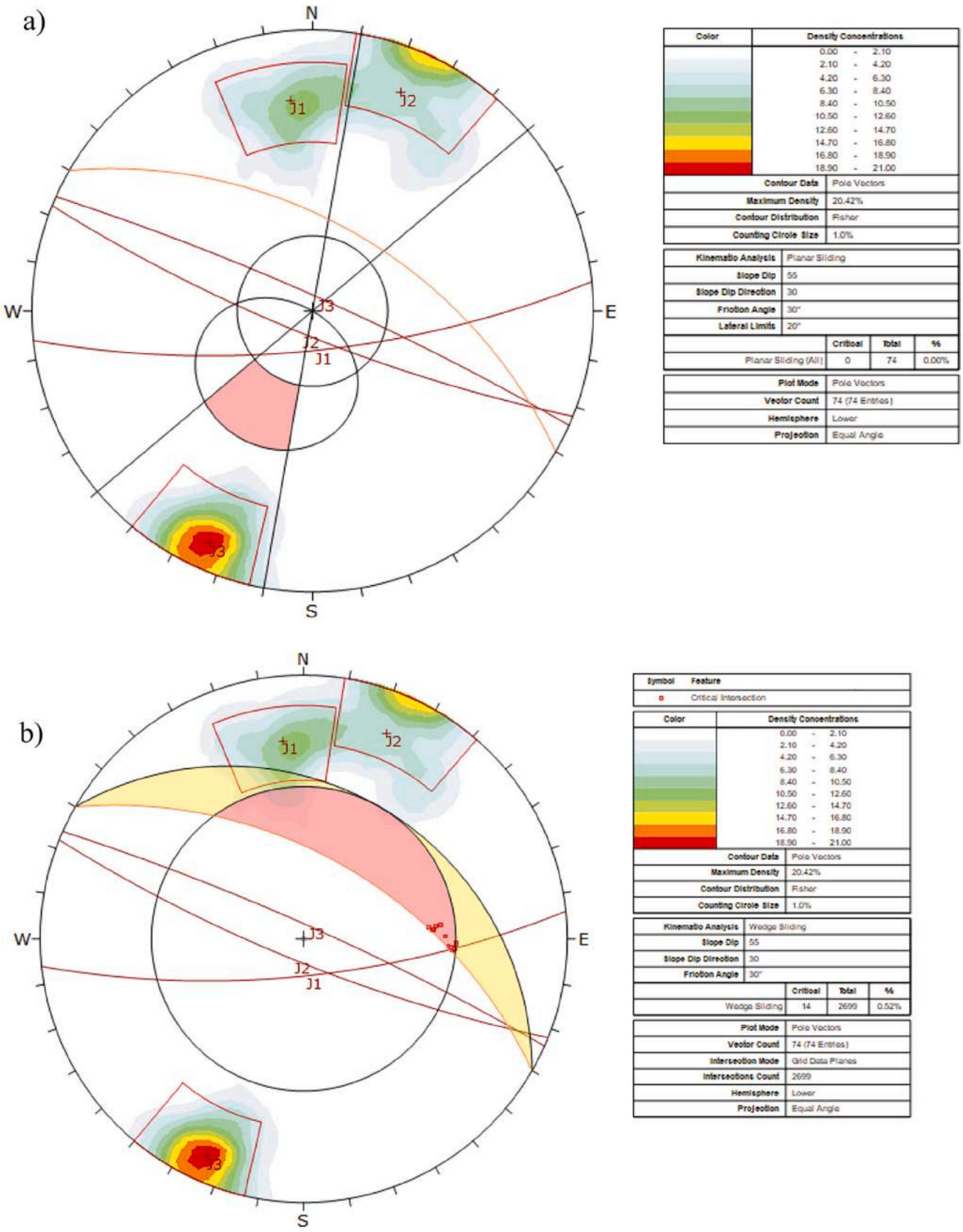

Fig. 11. Stereonet representation for various filures of right section of Site 1 a) sterenoet projection of planar failure b) stereonet projection of wedge failure.

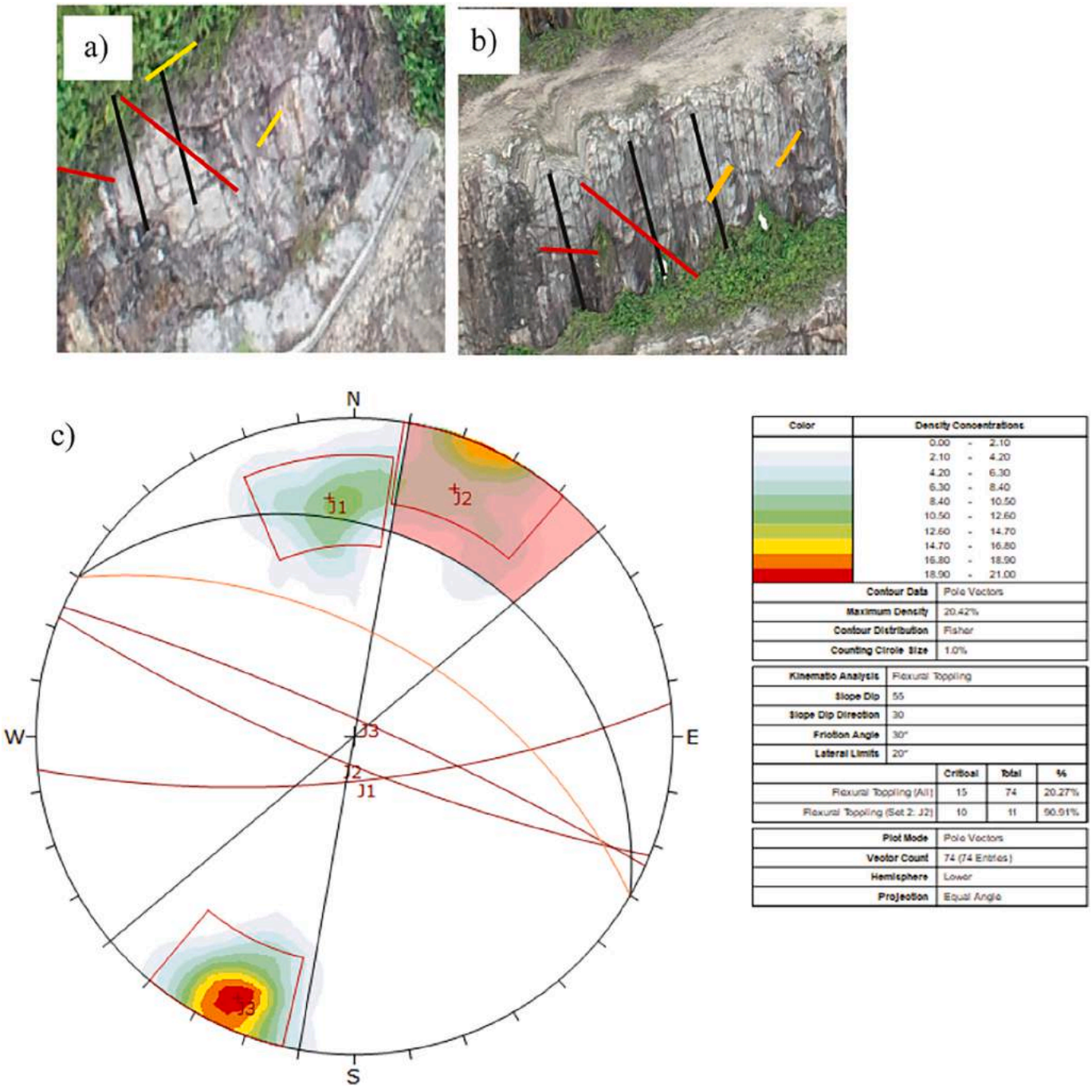

Fig. 12. Flexure toppling at right section of Site 1. a-b) flexure toppling on rock face.

site 2 ranges from 17.99 to 21.87; hence, the graphical representation for both equations is wider, representing the huge difference in RQD values (see Fig. 21b. This shows that the RQD values are quite sensitive to the Jv value especially for >10. Therefore, the selection of an appropriate equation is of utmost importance for the reliable calculation of RQD values. Eq. (2) is more appropriate for long or flat bars, whereas Eq. (3) is suitable for cubic bars (Zheng et al., 2020). In this research study, the Jv was calculated from flat bars; therefore, Eq. (2) is utilized for quantifying the rock mass quality. The RQD value of Site 1 ranges from 58 to 83, whereas Site 2 lies between 49 and 56. This demonstrates clearly that rock mass quality at Site 1 is fair to good, while at Site 2 is poor to fair rock based on the UAV survey.

The kinematic analysis successfully determines the possible failures on rock slope at both sites using a UAV 3D point cloud. The joints were efficiently clustered in various sets at both sites. At Site 1 J1 (74^0, 180^0) were found more dominantly while, at Site 2 J3 (26^0, 180^0) were found densely. Summarizing kinematic analysis, at Site 1 wedge and flexure failure are the primary failure mechanism, whereas, Site 2 is prone to only wedge failure. Furthermore, based on the kinematic analysis, particularly at Site 1 it is argued that the water saturation increases the risk of failure. It is due to an increase in the risk of planar and wedge observed in the left section of the slope compared to other sections at Site 1.

The accumulation of water in the subsurface rock mass and the high conductive lithological layers such as the clay layer also play a vital role in the rock fall triggering. Therefore, the delineation of subsurface geological features is also essential for the comprehensive assessment of rock slope instability. 2D ERT in this research work successfully

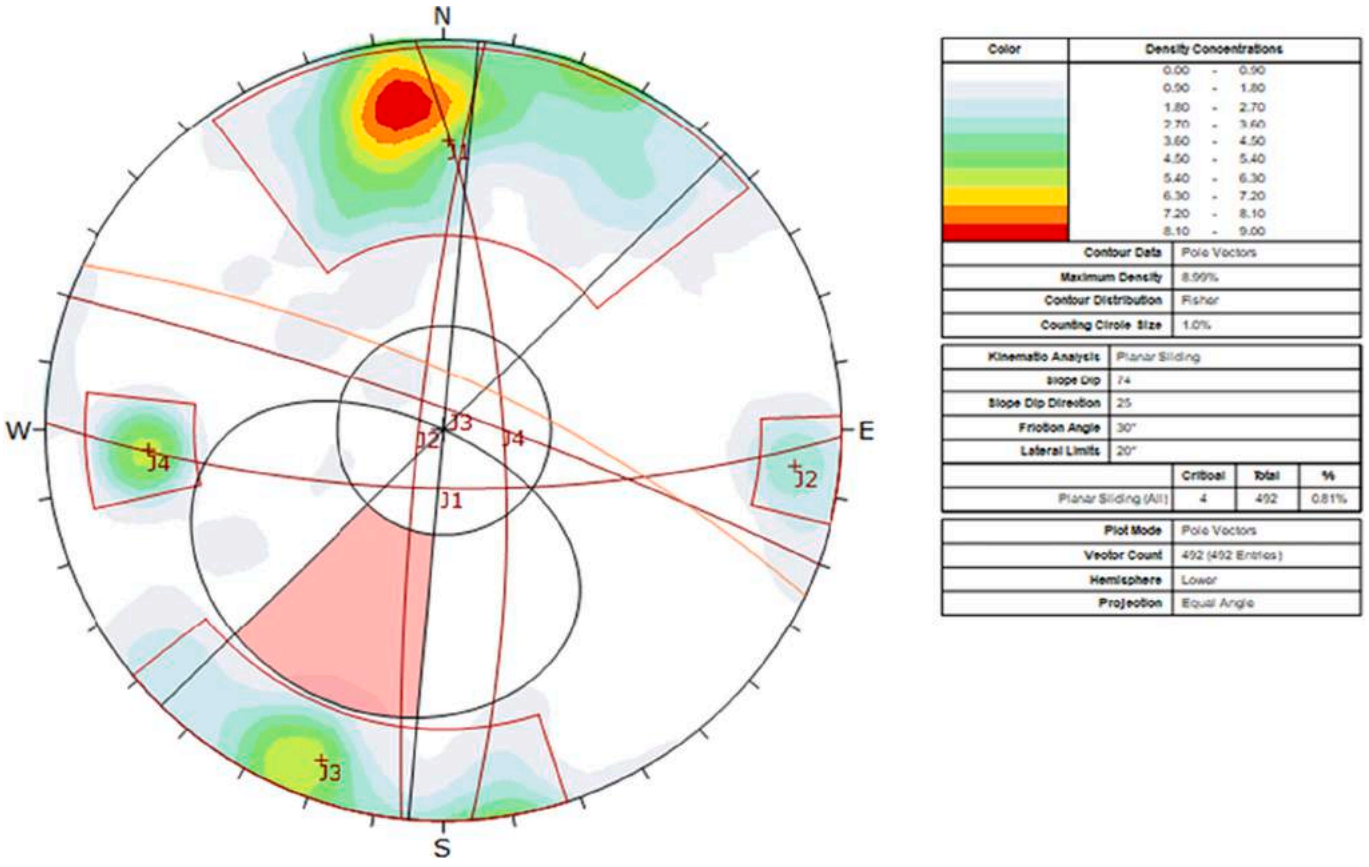

Fig. 13. Stereonet projection of planar failure at middle section of site 1.

characterizes the subsurface geology of rock slopes shown above in Fig. 9 and Fig. 10. Four lithological layers were identified by resistivity line L1 such as water-saturated layer, highly fracture, moderately fracture rock and fresh rock having resistivity values ranging 230 Ωm to >13,000 Ωm. Around 20 m thick layer of highly fractured rock at a depth of 40 m and 15 m were delineated towards southwest and northeast directions, respectively represented by green color. The yellow-coloured geological layer at the middle of the resistivity line refers to fractured rock having resistivity ranges 1000 Ωm to 2200 Ωm. Towards the Southwest direction fresh rock at depth of 15 m and 70 m having thickness 10 m and 20 m respectively were identified. The fresh rock is characterized as dark red color with resistivity values >2500 Ωm. A highly conductive geological layer 250 Ωm having a thickness of 15 m at 10 m depth towards the left of the slope was identified. This highly conductive layers refer to water-saturated zone as the runoff water on the slope surface towards the right was observed during the physical site visit and UAV survey as shown in Fig. 22(d).

A high proportion of fresh and strong rock mass was found by resistivity line L2 having resistivity values >2500 Ωm represented by dark red color. A highly fracture rock mass having resistivity values 500–1200 Ωm, represented by yellowish to green color with 40-45 m thickness was identified by 2D ERT survey towards northeast direction. Moderately fracture rock of resistivity ranges 1200–1800 Ωm characterized by yellow color at depth 30 m towards southwest direction was also identified. The subsurface beneath resistivity line L2 was found accumulated by water content towards the northeast direction and at the middle. The resistivity of this water saturated layer of ranges 250–350 Ωm having 10 to 20 m thickness. This high conductive layer is represented by dark blue color. The UAV 3D Point cloud also validate the 2D ERT results by identifying runoff water on the rock surface at the same location shown in Fig. 22(d). Furthermore, this low resistivity layer was reported by both resistivity lines L1 and L2 in the fracture rock mass. The presence of fracture granite rock around this low resistivity geological further confirms the presence of water saturated zone at Site 1. This area on the rock slope requires special attention as the presence of water in rock mass causes degradation of joint and discontinuities and triggered rock fall mechanism (Dochez et al., 2013). Based on the 2D ERT interpretation the substantial portion of the subsurface rock at Site 1 was found fresh rock.

The inverted images at Site 2 discern various subsurface geological layers having varying resistivity values. The yellowish color represents fractured granite having resistivity ranges 1000–2200 Ωm. A fresh granite rock layer at a depth of 5 m with a thickness of around 2 m having resistivity greater 2400 Ωm was characterized by dark red color. Immediate to the strong and fresh granite layer, a fracture granite layer of 1 m was also identified. The fractured granite is represented by yellowish color having resistivity ranges 1000–2200 Ωm. A highly fracture granite layer usually presents at depth of 10 m having resistivity ranges 400–1000 Ωm was identified throughout the study area. The resistivity layer represented with dark blue color shows the lowest resistivity values from 100 to 300 Ωm at 15 m depth. This layer is identified as clay layer. The 3D Point cloud of Site 2 also reported high clay content on rock face. The presence of clay on rock slope surface and in between joints were also observed visually during data collection.

This section provides a comparison of the efficacy of UAV and 2D ERT surveys based on the information obtained by both techniques required for slope stability assessment. The UAV successfully localized an existing planar failure covering an area of 30 m^2 on the top benches towards the northeast direction at Site 1 (Fig. 22c). The point cloud obtained from UAV images also proficiently located the runoff water on the rock face at Site 1, shown in Fig. 22d. The water on the rock slope was found towards the right end over an area of 4535.96 m^2. However, the efficiency of the UAV survey is highly affected by the presence of vegetation or any material on the rock face. At Site 1, the stability

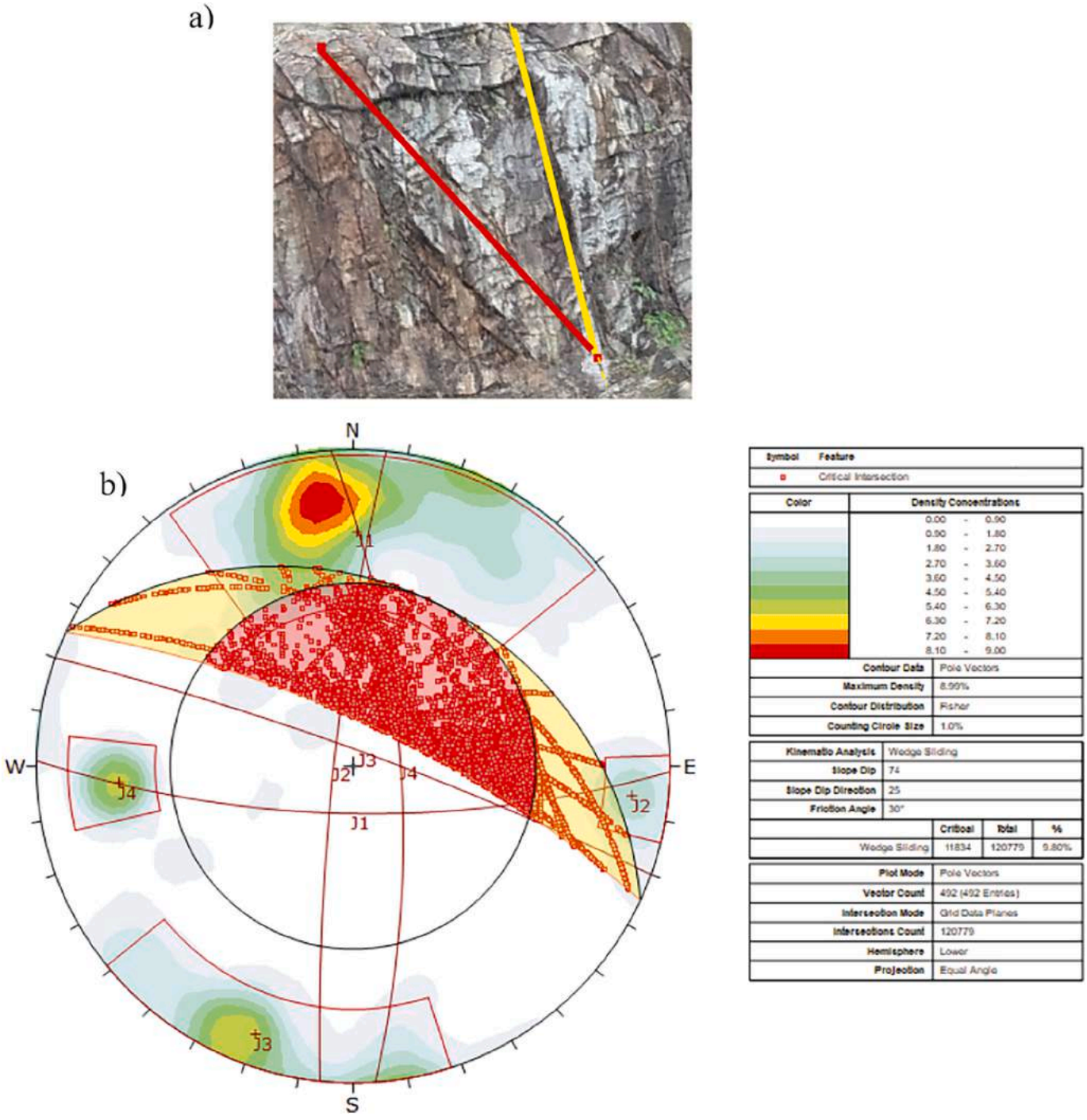

Fig. 14. Wedge failure at the middle section of Site 1 a) wedge failure on rock face b) Stereooet projection of wedge failure.

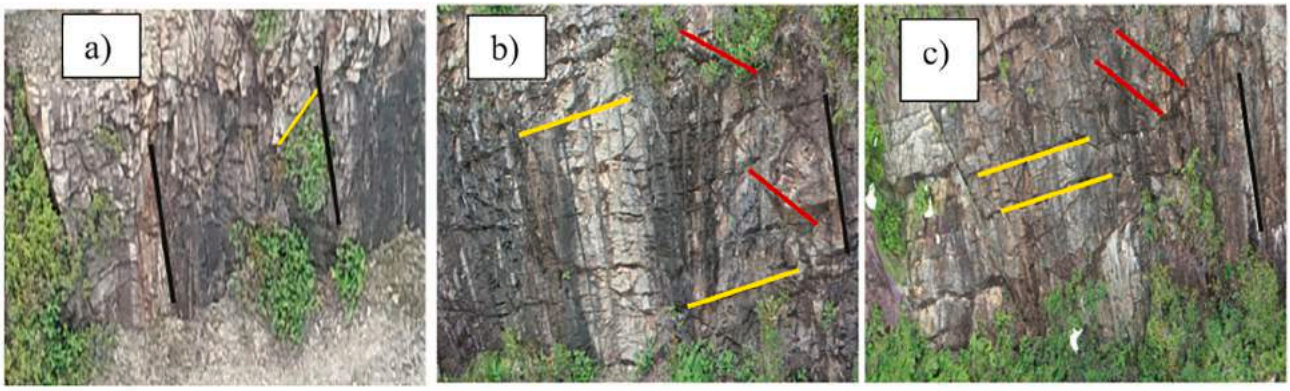

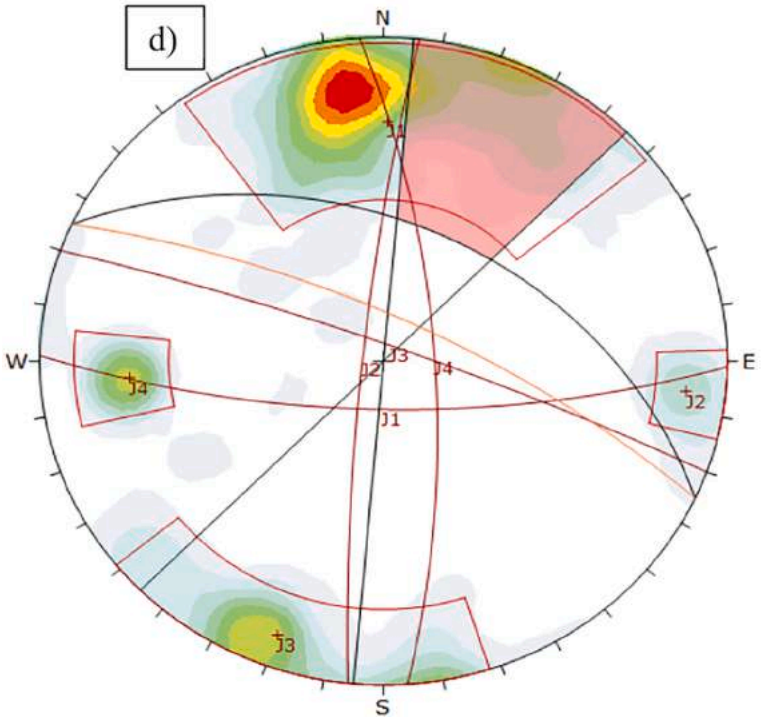

Color	Density Concentrations
	0.00 - 0.90
	0.90 - 1.80
	1.80 - 2.70
	2.70 - 3.60
	3.60 - 4.50
	4.50 - 5.40
	5.40 - 6.30
	6.30 - 7.20
	7.20 - 8.10
	8.10 - 9.00
Contour Data	Pole Vectors
Maximum Density	8.99%
Contour Distribution	Fisher
Counting Circle Size	1.0%

Kinematic Analysis	Flexural Toppling
Slope Dip	74
Slope Dip Direction	25
Friction Angle	30°
Lateral Limits	20°

	Critical	Total	%
Flexural Toppling (All)	68	492	13.82%
Flexural Toppling (Set 1, J1)	64	216	29.63%

Plot Mode	Pole Vectors
Vector Count	492 (492 Entries)
Hemisphere	Lower
Projection	Equal Angle

Fig. 15. Flexure toppling at the middle section of Site 1. a-c) flexure toppling on rock face d) Stereonet projection of flexure toppling.

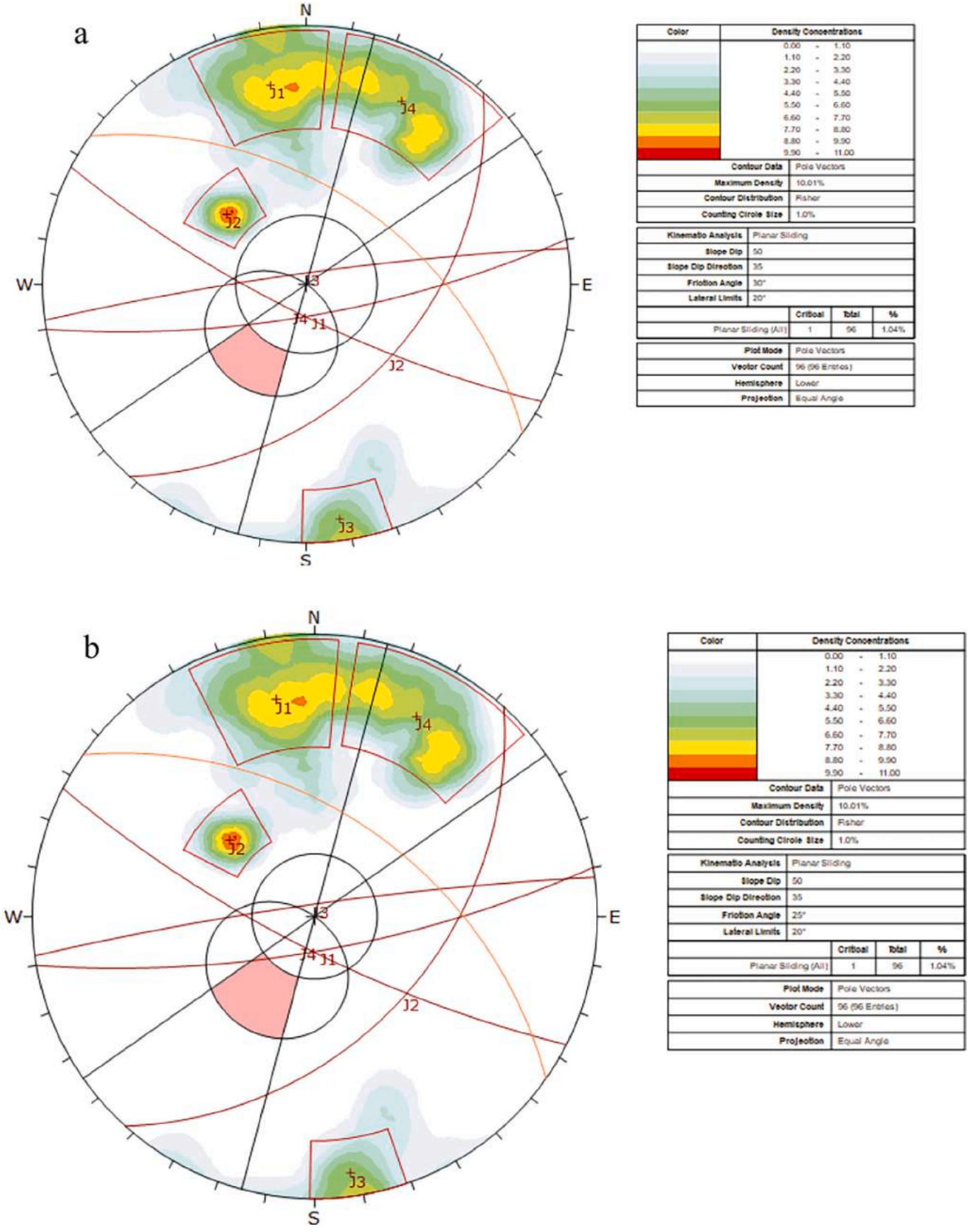

Fig. 16. Planar failure at the left section of Site 1. a) dry rock b) saturated rock.

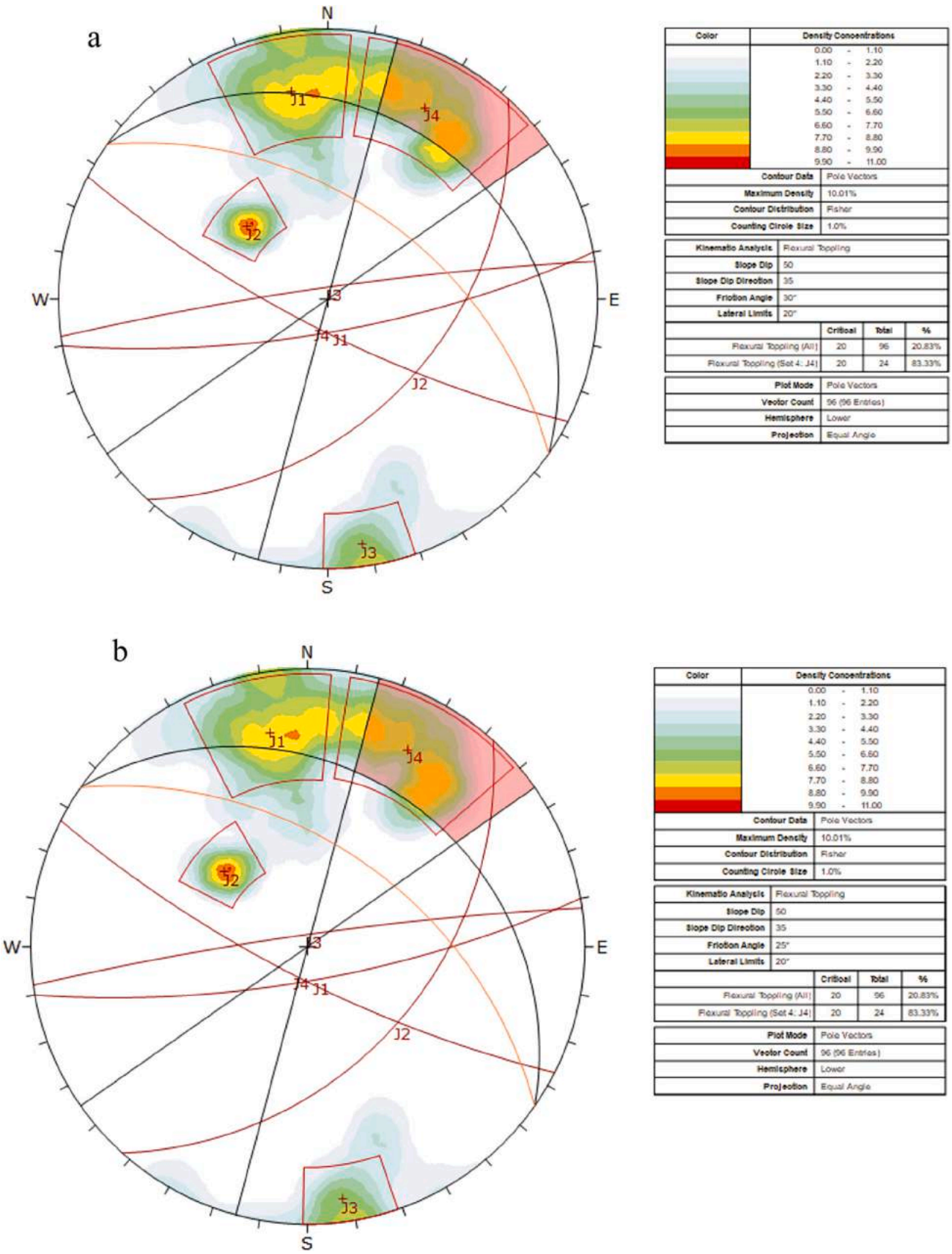

Fig. 17. Flexure toppling at the left section of Site 1. a) dry Rock b) saturated Rock.

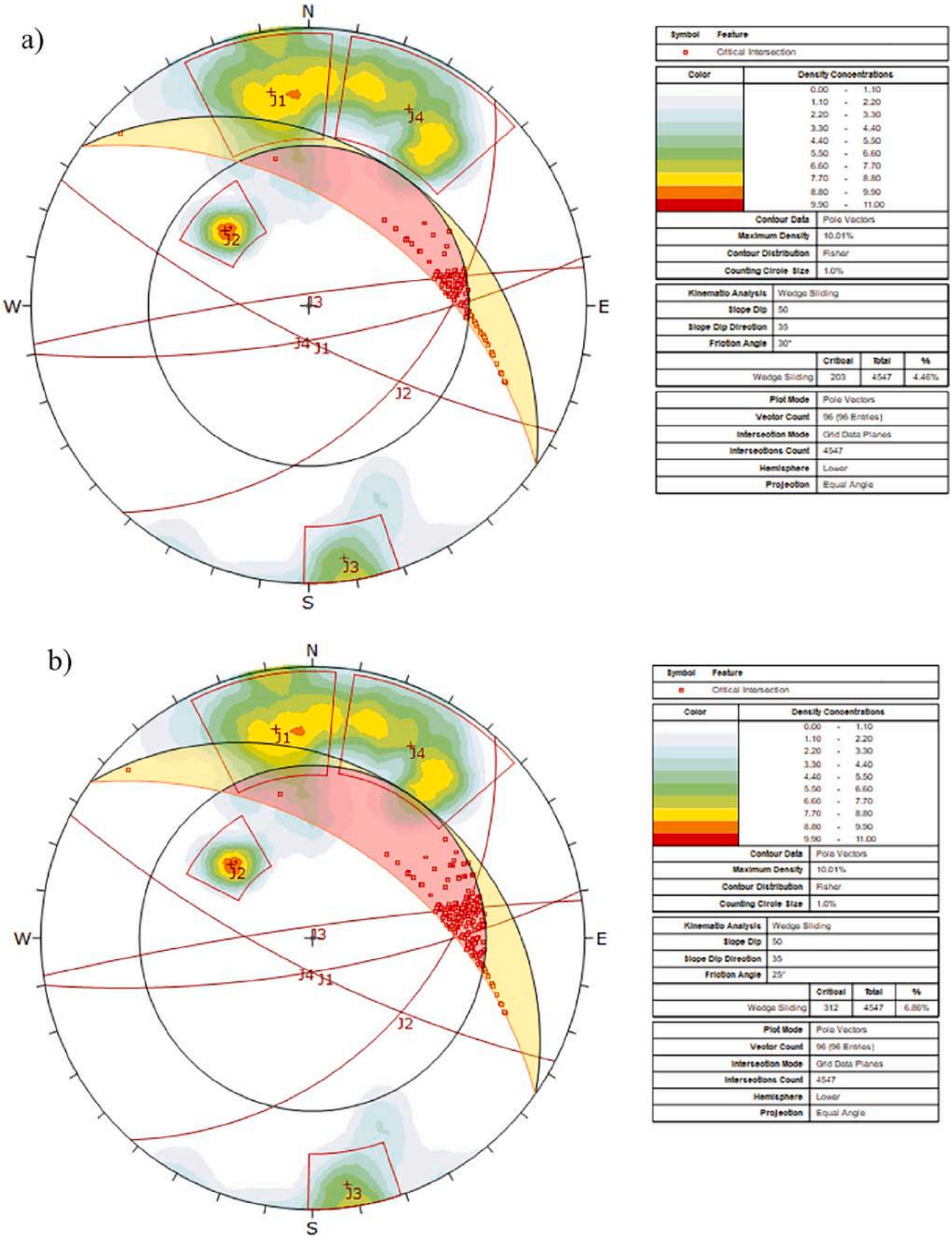

Fig. 18. Wedge failure at left section of Site 1. a) dry Rock b) saturated Rock.

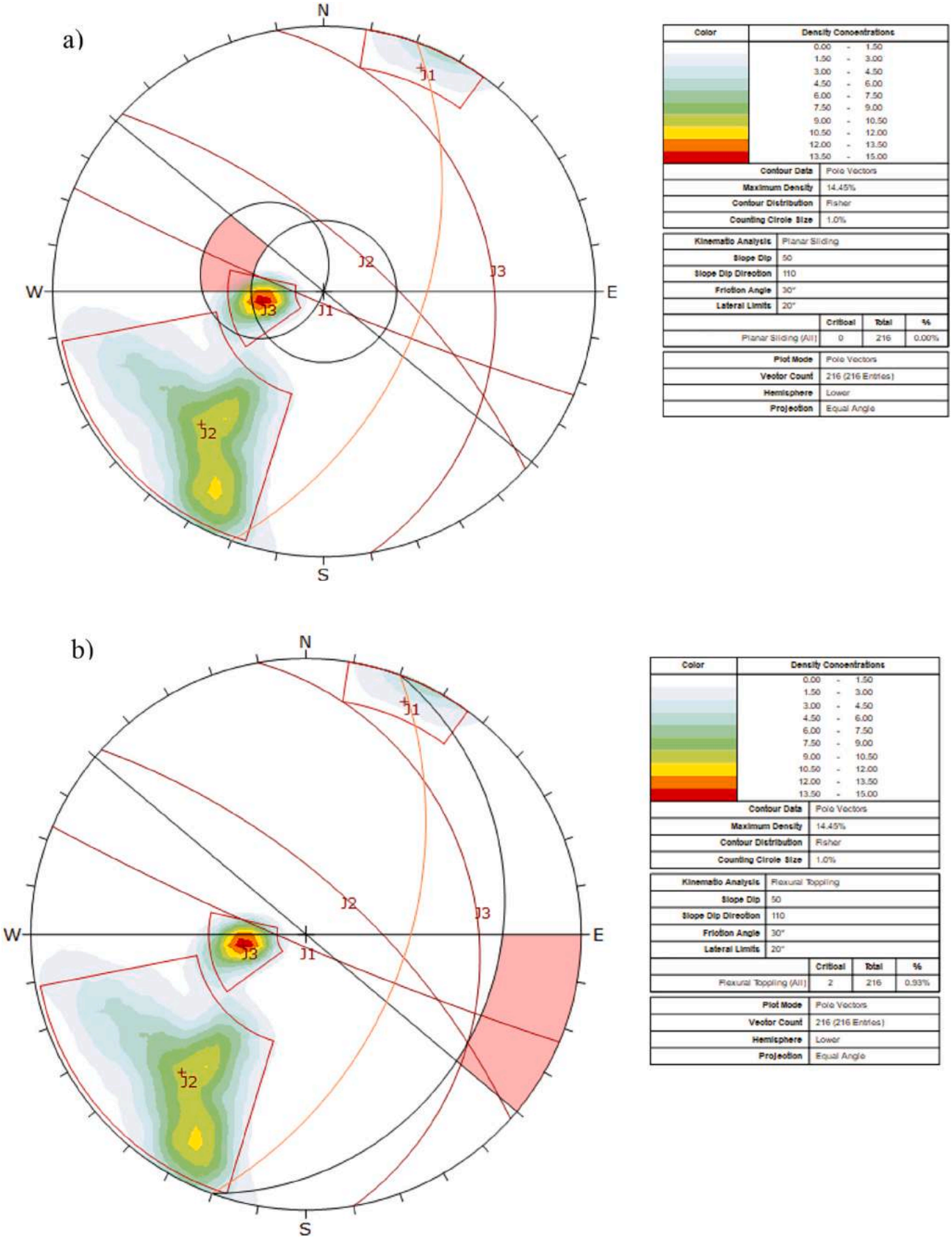

Fig. 19. Stereonet projection of Site 2 a) planar Failure, b) flexure Toppling.

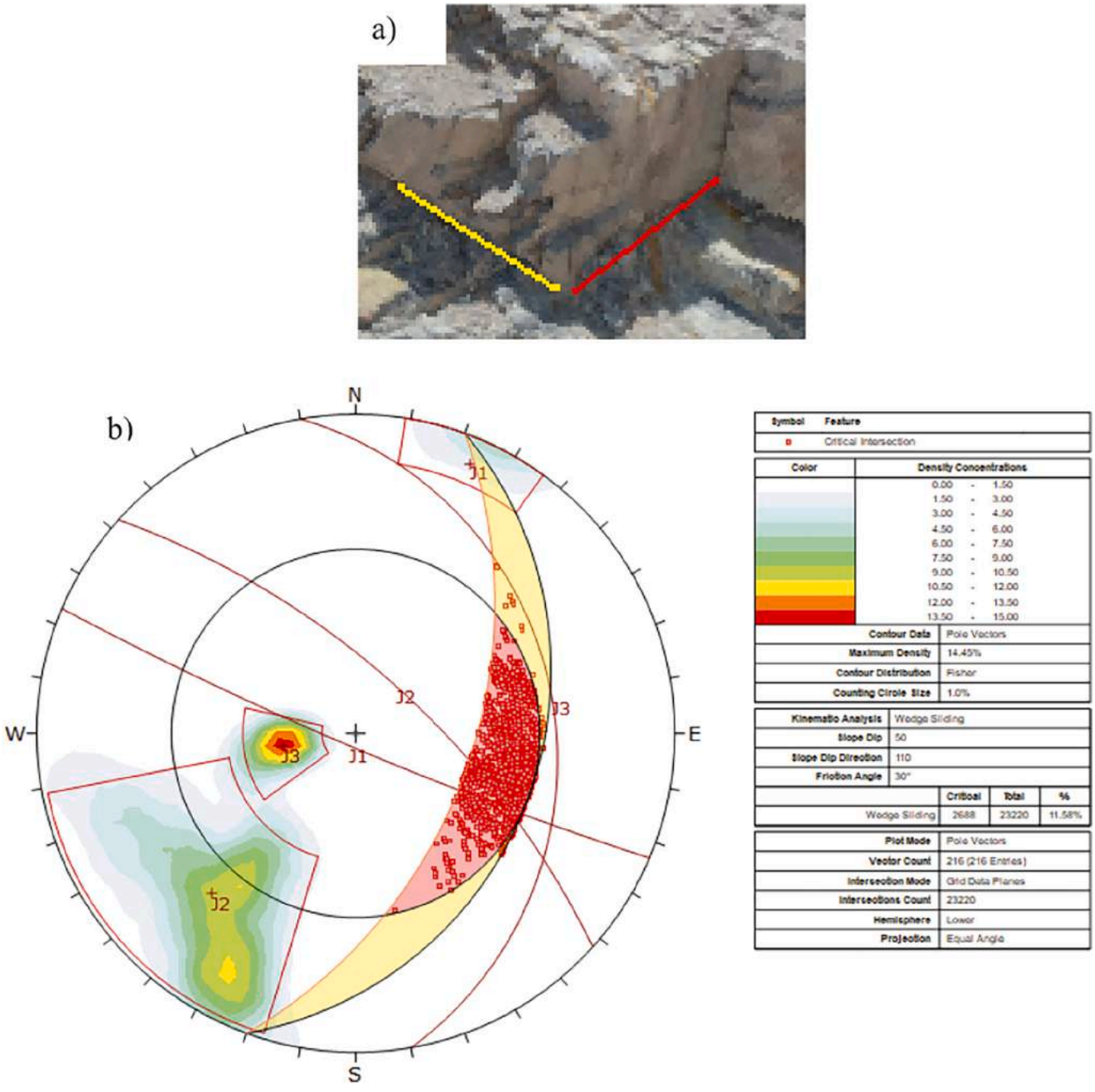

Fig. 20. a) Wedge failure on Rock Face b) Stereonet projection of wedge failure.

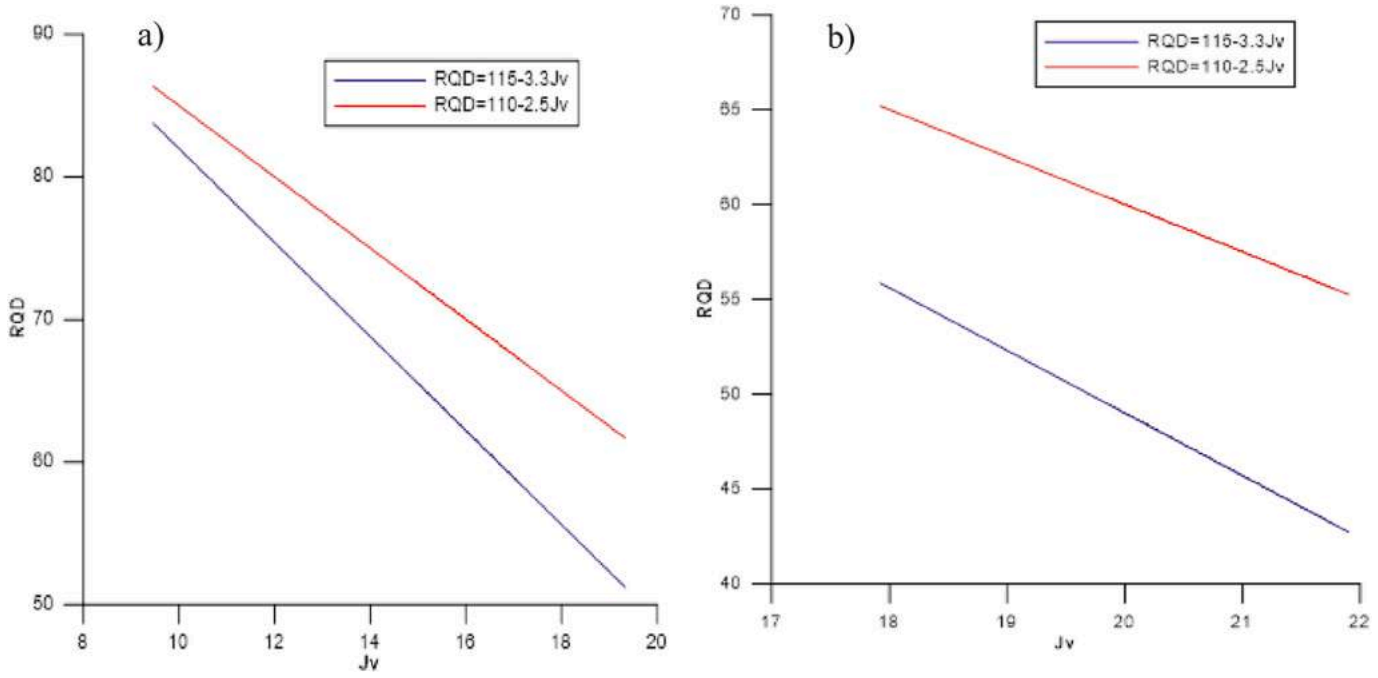

Fig. 21. RQD Calculation from Jv a) Site 1 b) Site 2.

assessment of 155,908.6 m^2 out of 264,373.9 was unable to perform using UAV images due to high vegetation on rock face. This area is 58% of the total slope area and is represented by a yellow circled area in Fig. 21a. The slope face at Site 2, particularly at the top was covered with loose material denoted by a yellow encircled area in Fig. 22b. This area is 34% of the total slope area, around 873.8 m^2 out of 2553.53 m^2. The rock mass condition of the rock outcrop at this area was not determined using a UAV point cloud. As shown in Fig. 22e, a degraded area of 124 m^2 was successfully identified by the UAV point cloud. The degraded rock face at Site 2 reveals the flow of water channel through this area during rainy days, which is alarming for any rock fall even in the future.

The 2D ERT survey provides the subsurface information in the form of a trapezoid. Therefore, some portion of the area of investigation that lies out of the trapezoid remains unidentified. The total coverage area of the 2D ERT survey of both lines L1 and L2 at Site 1 is represented by a marked red area in Fig. 21a. The total area covered by the 2D ERT survey is 156,361.74 $m^{2,}$ around 60% of the total slope area. This means at Site 1, 40% of the area remained unidentified by the 2D ERT survey. The 2D ERT survey at Site 2 was found highly efficient because only 4% that is 105.8 m^2 out of 2553.53 m^2 were not identified. By comparing the area of coverage of UAV and 2D ERT survey at both sites, 2D ERT was found efficient as it provided more information for more area than UAV.

Considering the socio-economic importance of both highways across Site 1 and Site 2, a comprehensive slope stability assessment is desired to mitigate anticipated rock fall event. For this purpose, an integrated 2D ERT and UAV survey was carried out at both sites. Based on the obtained RQD value from various sections at Site 1 the quality of the rock is fair to good. On the contrary, the quality of rock at Site 2 based on RQD was identified as poor. The resistivity survey also confirms that the subsurface rock mass at Site 1 is moderately fractured, while at Site 2 is highly fractured. The kinematic analysis of the UAV survey of Site 1 reveals that 0.4% of the total slope area is prone to various types of failure. The discontinuity orientations at Site 1 are more prone to flexure toppling and wedge failure. The interesting observation from the UAV point cloud is that the rock slope at the top was found to be more fractured than the lower portion. The same trend was also noticed in the 2D ERT images. A high proportion of the fractured rock was identified by resistivity Line L1 as compared to resistivity Line L2. At Site 1, a runoff water covering around 1.7% of the slope area towards the north-east direction on the left section was located by UAV images. The resistivity Line 2 also delineates water accumulation in subsurface rock mass in the northeast direction. This means that the runoff water present at Site 1 is not limited to the rock surface but infiltered to the subsurface rock mass. This area needs attention to avoid any future rock fall, even as water infiltration in subsurface rock mass plays a key role in the degradation of the rock mass that results in rock slope failure. The integrated 2D ERT and UAV approach in this research work was efficient, inexpensive, expeditious and environmentally friendly for slope stability assessment.

6. Conclusion

Integrated application of 2D ERT and UAV allowed a detailed and comprehensive assessment of the rock slope at both sites. The point cloud reconstructed from the UAV survey enables the calculation of RQD from the 3D point cloud, thus allowing the quantification of rock mass quality. Based on obtained RQD, the rock quality at Site 1 was fair to good rock, while at Site 2 was a poor rock.

The UAV survey also helps to extract discontinuity orientations that enabled to perform the kinematic analysis of the rock slope. Based on the UAV point cloud, the rock slope at Site 1 was highly prone to flexural toppling, while few intersections resulted in the geometrical formation of wedge failure. The UAV survey also identified an existing planar failure on the rock top along with the runoff water at Site 1. At Site 2, wedge failure was found to be the dominant failure.

The 2D ERT survey also successfully identified various subsurface lithological features efficiently. Based on a 2D ERT survey, the subsurface rock mass at Site 1 was reported fractured to fresh rock. Whereas, at Site 2, on the top, a 10 m thick layer of fresh rock was identified by resistivity survey. However, the greater portion of the rock mass at Site 2 was reported to be highly fractured.

Comparing 2D ERT and UAV surveys, UAV at Site 1 fails to provide information of 58% of the slope area and 34% at Site 2 due to high vegetation and loose rock on the rock slope. In the contrary, the unidentified subsurface geology by 2D ERT was 40% and 4% at Site 1 and Site 2, respectively. However, the combined application of 2D ERT and

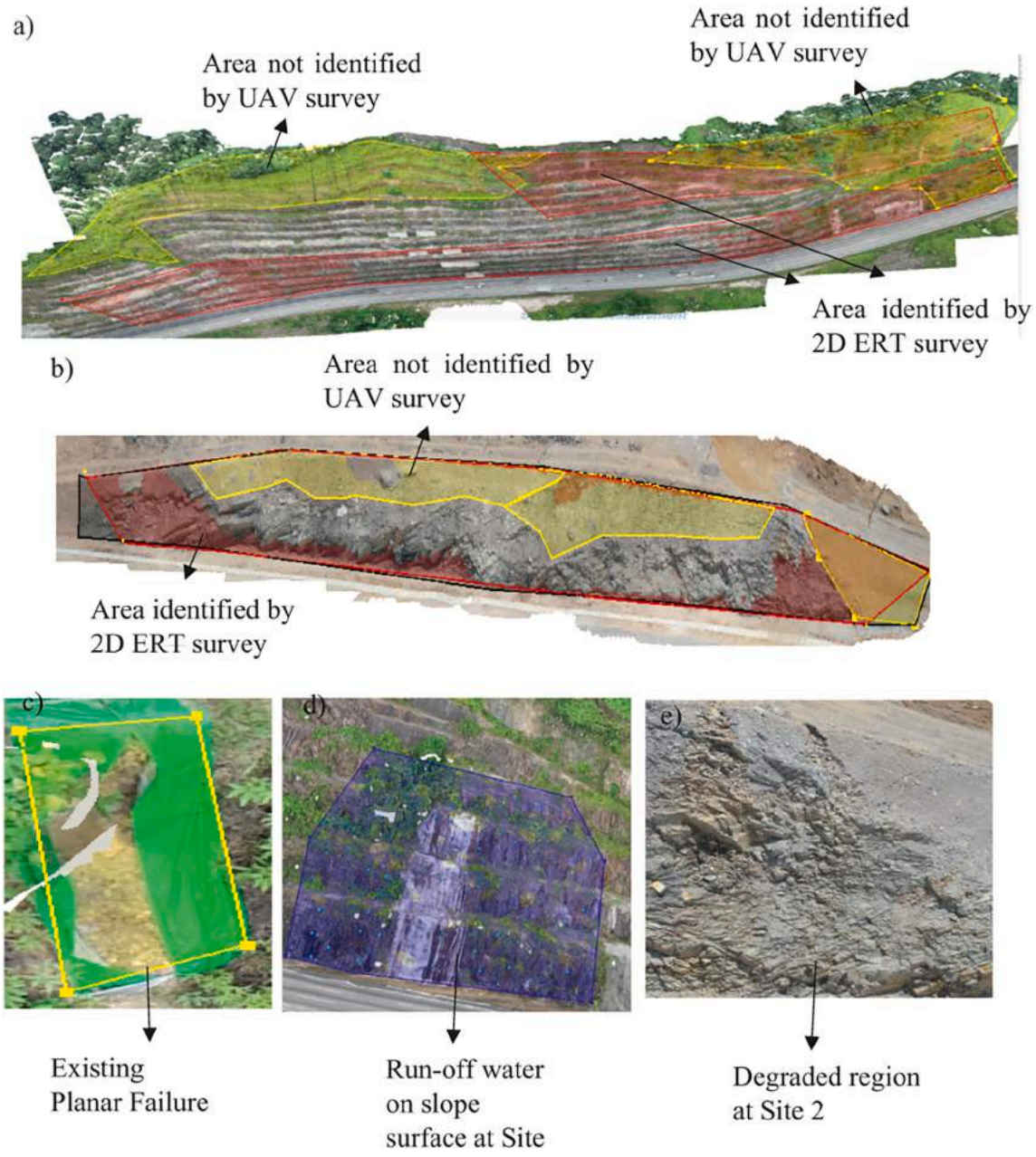

Fig. 22. a) Area coverage by 2D ERT and UAV at Site 1 b) area coverage by 2D ERT and UAV at Site 2 c) existing planar failure at Site 1 d) runoff water at Site 1 e) degraded rock mass on slope face at Site 2.

UAV allows the detail assessment of the rock slope at both sites. The integrated 2D ERT and UAV approach is expeditious, inexpensive and rapid for comprehensive slope stability assessment. Furthermore, the surface and subsurface rock mass quality was successfully analyzed by integrated UAV and 2D ERT approach without any environmentally degradation.

CRediT authorship contribution statement

Muhammad Junaid: Conceptualization, Writing – original draft, Methodology, Software. **Rini Asnida Abdullah:** Writing – review & editing, Supervision, Funding acquisition. **Radzuan Saa'ri:** Project administration, Writing – review & editing. **Mohd Nur Asmawisham Alel:** Validation.

Declaration of Competing Interest

The authors have no conflict of interest.

Acknowledgments

The research work was jointly funded by the higher education Commission (HEC) Pakistan under HRD scheme and Universiti Teknologi Malaysia under grant Q.J130000.2651.16J25. The authors also extend special thanks to the 3GSM for providing the complimentary educational license of the SMX UAV software.

References

3GSM. Retrieved from. https://3gsm.at/.
Abdullah RA. Development of a slope classification system with particular reference to shallow rock slope failure. (PhD Thesis). The University of Leeds.

Alameda-Hernández, P., El Hamdouni, R., Irigaray, C., Chacón, J., 2019. Weak foliated rock slope stability analysis with ultra-close-range terrestrial digital photogrammetry. Bull. Eng. Geol. Environ. 78 (2), 1157–1171. https://doi.org/10.1007/s10064-017-1119-z.
Albarelli, D., Mavrouli, O., Nyktas, P., 2021. Identification of potential rockfall sources using UAV-derived point cloud. Bull. Eng. Geol. Environ. 1–23.
Awang, H., Salmanfarsi, A., Misbahuddin, A., Ali, M., 2021. Slope stability analysis of rock mass using Rock Mass Rating and Slope Mass Rating. In: Paper presented at the IOP Conference Series: Earth and Environmental Science.
Azarafza, M., Nanehkaran, Y.A., Rajabion, L., Akgün, H., Rahnamarad, J., Derakhshani, R., Raoof, A., 2020. Application of the modified Q-slope classification system for sedimentary rock slope stability assessment in Iran. Eng. Geol. 264, 105349.
Bar, N., Kostadinovski, M., Tucker, M., Byng, G., Rachmatullah, R., Maldonado, A., Yacoub, T., 2020. Rapid and robust slope failure appraisal using aerial photogrammetry and 3D slope stability models. Int. J. Min. Sci. Technol.
Barlow, J., Gilham, J., Ibarra Cofrã, I., 2017. Kinematic analysis of sea cliff stability using UAV photogrammetry. Int. J. Remote Sens. 38 (8–10), 2464–2479.
Barton, N., Choubey, V., 1977. The shear strength of rock joints in theory and practice. Rock Mech. 10 (1), 1–54.
Buša, J., Rusnák, M., Kušnirák, D., Greif, V., Bednarik, M., Putiška, R., Rusnáková, D., 2020. Urban landslide monitoring by combined use of multiple methodologies-a case study on Sv. Anton town, Slovakia. Phys. Geogr. 41 (2), 169–194.
Chen, Q., Yin, T., 2019. Should the use of rock quality designation be discontinued in the rock mass rating system? Rock Mech. Rock. Eng. 52 (4), 1075–1094.
CM, C., 2014. Structural History of the Kinta Valley. MSc Thesis. Geoscience Dept., Faculty of Geoscience and Petroleum.
Colomina, I., Molina, P., 2014. Unmanned aerial systems for photogrammetry and remote sensing: a review. ISPRS J. Photogramm. Remote Sens. 92, 79–97 dji. Retrieved from. https://www.dji.com/phantom-4-pro-v2.
Dochez, S., Laouafa, F., Franck, C., Guedon, S., Martineau, F., Bost, M., D'Amato, J., 2013. Influence of water on rock discontinuities and stability of rock mass. Proc. Earth Planet. Sci. 7, 219–222.
Egwuonwu, G., Okoyeh, E., Agarana, D., Nwaka, E., Nwosu, O., Chikwelu, E., 2021. Preliminary gully hazard assessment using 2D-ERT and 2D-SRT geophysical surveys: a Case study in southeastern Nigeria, 7 (3).
Ekinci, A., Muturi, T., Ferreira, P.M.V., 2021. Aerial close-range photogrammetry to quantify deformations of the pile retaining walls. J. Ind. Soc. Remote Sens. 49 (5), 1051–1066.
Erguler, Z.A., Karakuş, H., Ediz, İ.G., Şensöğüt, C., 2020. Assessment of design parameters and the slope stability analysis of weak clay-bearing rock masses and associated spoil piles at Tunçbilek basin. Arab. J. Geosci. 13 (1), 1–11.
Falae, P.O., Kanungo, D.P., Chauhan, P.K.S., Dash, R.K., 2019. Electrical resistivity tomography (ERT) based subsurface characterization of Pakhi Landslide, Garhwal Himalayas, India. Environ. Earth Sci. 78 (14), 430.
Guisado-Pintado, E., Jackson, D.W., Rogers, D., 2019. 3D mapping efficacy of a drone and terrestrial laser scanner over a temperate beach-dune zone. Geomorphology 328, 157–172.
Gurocak, Z., Alemdag, S., Zaman, M.M., 2008. Rock slope stability and excavatability assessment of rocks at the Kapikaya dam site, Turkey. Eng. Geol. 96 (1–2), 17–27.
Haftani, M., Chehreh, H.A., Mehinrad, A., Binazadeh, K., 2016. Practical investigations on use of weighted joint density to decrease the limitations of RQD measurements. Rock Mech. Rock. Eng. 49 (4), 1551–1558.
Haliza Abdul Rahmana, J.M., 2017. Landslides disaster in Malaysia: an overview. Health Environ. J. 8 (1), 13.
Ibraheem, I.M., Tezkan, B., Bergers, R., 2021. Integrated interpretation of magnetic and ERT data to characterize a landfill in the north-west of Cologne, Germany. Pure Appl. Geophys. 1–22.
Ishak, M.F., Zaini, M.I., Zolkepli, M., Wahap, M., Sidek, J.J., Yasin, A.M., Talib, Z.A., 2020. Granite exploration by using electrical resistivity imaging (ERI): a case study in Johor. Int. J. Integr. Eng. 12 (8), 328–347.
(JMG), M.a.G.d., 2014. Geological map of peninsular Malaysia. (Peta Geologi Semenanjung). Retrieved from. https://www.jmg.gov.my/add_on/mt/smnjg/tiles/.
Junaid, M., Abdullah, R.A., Saa'ri, R., Alel, M., Ali, W., Ullah, A., 2019. Recognition of Boulder in Granite Deposit Using Integrated Borehole and 2D Electrical Resistivity Imaging for Effective Mine Planning and Development.
Junaid, M., Abdullah, R.A., Sa'ari, R., Ali, W., Rehman, H., Alel, M.N.A., Ghani, U., 2021. 2d electrical resistivity tomography an advance and expeditious exploration technique for current challenges to mineral industry. J. Himal. Earth Sci. 54 (1), 11–32. Retrieved from. https://www.scopus.com/inward/record.uri?eid=2-s2.0-85104835810&partnerID=40&md5=eda7de5783a117d973896adcd34f2f27.
Khan, M.S., Hossain, S., Ahmed, A., Faysal, M., 2017. Investigation of a shallow slope failure on expansive clay in Texas. Eng. Geol. 219, 118–129.
Khanna, R., Dubey, R., 2021. Comparative assessment of slope stability along road-cuts through rock slope classification systems in Kullu Himalayas, Himachal Pradesh, India. Bull. Eng. Geol. Environ. 80 (2), 993–1017.
Kumari, A., Kumar, D., Warwade, P., 2021. Application of multi-criteria decision making (MCDM) and electrical resistivity tomography (ERT) techniques for identification of groundwater recharge zone (s) in granitic hard rock aquifer. J. Earth Syst. Sci. 130 (2), 1–17.
Lee, S., Choi, Y., 2016. Reviews of unmanned aerial vehicle (drone) technology trends and its applications in the mining industry. Geosyst. Eng. 19 (4), 197–204.
Lin, D., Yuan, R., Lin, X., Lin, X., Lou, C., Cai, Y., Wang, H., 2021. Disturbed granite identification by integrating rock mass geophysical properties. Int. J. Rock Mech. Min. Sci. 138, 104596.
Loke, M., 1999. A practical guide to Electrical imaging surveys for environmental and engineering studies. Tutorial 2, 70.
Loke, M., Chambers, J., Rucker, D., Kuras, O., Wilkinson, P., 2013. Recent developments in the direct-current geoelectrical imaging method. J. Appl. Geophys. 95, 135–156.
Mezerreg, N.E.H., Kessasra, F., Bouftouha, Y., Bouabdallah, H., Bollot, N., Baghdad, A., Bougdal, R., 2019. Integrated geotechnical and geophysical investigations in a landslide site at Jijel, Algeria. J. Afric. Earth Sci. 160, 103633.
Morales, M., Panthi, K.K., Botsialas, K., 2019. Slope stability assessment of an open pit mine using three-dimensional rock mass modeling. Bull. Eng. Geol. Environ. 78 (2), 1249–1264.
Nanda, A.M., Yousuf, M., Islam, Z.U., Ahmed, P., Kanth, T., 2020. Slope stability analysis along NH 1D from Sonamarg to Kargil, J&K, India: implications for landslide risk reduction. J. Geol. Soc. India 96 (5), 499–506.
Olona, J., Pulgar, J.A., Fernández-Viejo, G., López-Fernández, C., González-Cortina, J.M., 2010. Weathering variations in a granitic massif and related geotechnical properties through seismic and electrical resistivity methods. Near Surf. Geophys. 8 (6), 585–599.
Park, S., Choi, Y., 2020. Applications of unmanned aerial vehicles in mining from exploration to reclamation: a review. Minerals 10 (8), 663.
Park, H.-J., Lee, J.-H., Kim, K.-M., Um, J.-G., 2016. Assessment of rock slope stability using GIS-based probabilistic kinematic analysis. Eng. Geol. 203, 56–69.
Pasierb, B., Grodecki, M., Gwóźdź, R., 2019. Geophysical and geotechnical approach to a landslide stability assessment: a case study. Acta Geophys. 67 (6), 1823–1834.
Rahman, H.A., Mapjabil, J., 2017. Landslides disaster in Malaysia: an overview. Health 8 (1), 58–71.
Rocsciences. Retrieved from. https://www.rocscience.com/.
Rodriguez, J., Macciotta, R., Hendry, M., Roustaei, M., Gräpel, C., Skirrow, R., 2020. UAVs for monitoring, investigation, and mitigation design of a rock slope with multiple failure mechanisms—a case study. Landslides.
Rusydy, I., Fathani, T.F., Al-Huda, N., Iqbal, K., Jamaluddin, K., Meilianda, E., 2021. Integrated approach in studying rock and soil slope stability in a tropical and active tectonic country. Environ. Earth Sci. 80 (2), 1–20.
Sadeghi, S., Teshnizi, E.S., Ghoreishi, B., 2020. Correlations between various rock mass classification/characterization systems for the Zagros tunnel-W Iran. J. Mt. Sci. 17 (7), 1790–1806.
Samodra, G., Ramadhan, M. F., Sartohadi, J., & Anggri, M. Characterization of displacement and internal structure of landslides from multitemporal UAV and ERT imagings.
Sari, M., Seren, A., Alemdag, S., 2020. Determination of geological structures by geophysical and geotechnical techniques in Kırklartepe Dam Site (Turkey). J. Appl. Geophys. 182, 104174.
Singh, H.O., Ansari, T.A., Singh, T., Singh, K., 2020. Analytical and numerical stability analysis of road cut slopes in Garhwal Himalaya, India. Geotech. Geol. Eng. 38, 4811–4829.
Smith, J.V., Holden, L., 2021. Rock slope kinematic instability controlled by large-scale variation of basalt column orientation. Bull. Eng. Geol. Environ. 80 (1), 239–250.
Török, Á., Barsi, Á., Bögöly, G., Lovas, T., Somogyi, Á., Görög, P., 2018. Slope stability and rockfall assessment of volcanic tuffs using RPAS with 2-D FEM slope modelling. Nat. Hazards Earth Syst. Sci. 18 (2).
Vanneschi, C., Eyre, M., Burda, J., Žižka, L., Francioni, M., Coggan, J.S., 2018. Investigation of landslide failure mechanisms adjacent to lignite mining operations in North Bohemia (Czech Republic) through a limit equilibrium/finite element modelling approach. Geomorphology 320, 142–153.
Wang, S., Zhang, Z., Wang, C., Zhu, C., Ren, Y., 2019a. Multistep rocky slope stability analysis based on unmanned aerial vehicle photogrammetry. Environ. Earth Sci. 78 (8), 260.
Wang, S.H., Ahmed, Z., Z. H. H., & Pengy, W., 2019b. Cliff face rock slope stability analysis based on unmanned arial vehicle (UAV) photogrammetry. Geomech. Geophys. Geo-Energy and Geo-Resour. 5 (4), 333–344. https://doi.org/10.1007/s40948-019-00107-2.
Zhang, L., Einstein, H., 2004. Using RQD to estimate the deformation modulus of rock masses. Int. J. Rock Mech. Mining Sci. (1997) 41 (2), 337–341.
Zhang, W., Wang, Q., Chen, J.-p., Tan, C., Yuan, X.-q, 2012. Determination of the optimal threshold and length measurements for RQD calculations. Int. J. Rock Mech. Min. Sci. 1997 (51), 1–12.
Zheng, J., Yang, X., Lü, Q., Zhao, Y., Deng, J., Ding, Z., 2018. A new perspective for the directivity of rock quality designation (RQD) and an anisotropy index of jointing degree for rock masses. Eng. Geol. 240, 81–94.
Zheng, J., Wang, X., Lü, Q., Liu, J., Guo, J., Liu, T., Deng, J., 2020. A contribution to relationship between volumetric joint count (J v) and rock quality designation (RQD) in three-dimensional (3-D) space. Rock Mech. Rock. Eng. 53 (3), 1485–1494.
Zond. Retrieved from. http://zond-geo.com/english/.